Quantitative Evaluation of a Multimodal Aptamer-Targeted Long-Circulating Polymer for Tumor Targeting

Lennart Bohrmann, Tobias Burghardt, Cristina Rodríguez-Rodríguez, Matthias M. Herth, Katayoun Saatchi,* and Urs O. Häfeli*

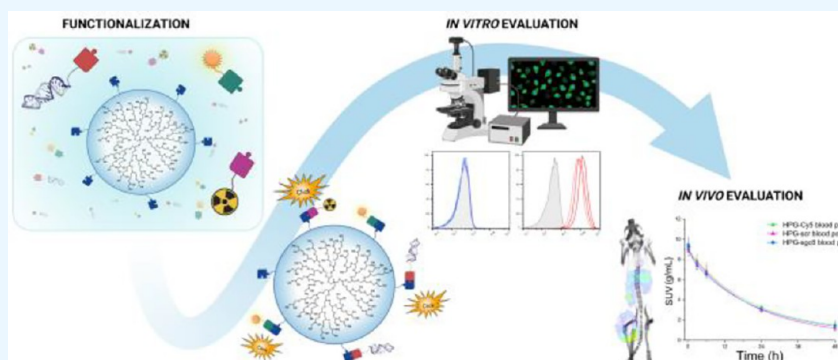Cite This: *ACS Omega* 2023, 8, 11003−11020

Read Online

ACCESS | Metrics & More | Article Recommendations | Supporting Information

ABSTRACT: Aptamers are promising targeting agents for imaging and therapy of numerous diseases, including cancer. However, a significant shortcoming of aptamers is their poor stability and fast excretion, limiting their application in vivo. Common strategies to overcome these challenges is to chemically modify aptamers in order to increase their stability and/or to apply formulation technologies such as conjugating them to polymers or nanocarriers in order to increase their circulation half-life. This is expected to result in improved cellular uptake or retention to passively targeted nanomedicines. Herein, we report a modular conjugation strategy based on click chemistry between functionalized tetrazines and *trans*-cyclooctene (TCO), for the modification of high molecular weight hyperbranched polyglycerol (HPG) with sgc8 aptamer, fluorescent dyes, and [111]In. Our data indicate strong affinity of sgc8 against a range of solid tumor-derived cell lines that have previously not been tested with this aptamer. Nevertheless, nonspecific uptake of scrambled ssDNA-functionalized HPG in cells highlights inherent challenges of aptamer-targeted probes that remain to be solved for clinical translation. We validate HPG-sgc8 as a nontoxic nanoprobe with high affinity against MDA-MB-468 breast and A431 lung cancer cells and show significantly increased plasma stability compared to free sgc8. In vivo quantitative SPECT/CT imaging indicates EPR-mediated tumor uptake of HPG-sgc8 and nontargeted or scrambled ssDNA-conjugated HPG but no statistically significant difference between these formulations in terms of total tumor uptake or retention. Our study emphasizes the need for stringent controls and quantification in the evaluation of aptamer-targeted probes. For this purpose, our versatile synthesis strategy provides a simple approach for the design and evaluation of long-circulating aptamer-conjugated nanoformulations.

INTRODUCTION

In recent years, nanotechnology has emerged as a powerful tool for the design of molecular imaging probes for the diagnosis and therapy for a variety of diseases. A substantial advantage of nanoparticles (NPs) such as liposomes, polymers, micelles, metal NPs, and dendrimers over smaller targeting vectors like biomolecules and small molecules is their eligibility for functionalization with a plethora of functional groups to afford multimodal diagnostic or therapeutic probes.[1,2] Generally, molecular imaging probes consist of a targeting vector that is able to bind to a disease-specific marker with high affinity and specificity and is linked to a reporter molecule that allows for direct or indirect tracking of the probe in vivo. Using NPs as carrier for both targeting moiety and reporter

molecule(s) offers several advantages over smaller imaging probes such as prolonged circulation, higher signal intensity, multimodal imaging capabilities, and additional space for payloads for theranostic applications.[3,4]

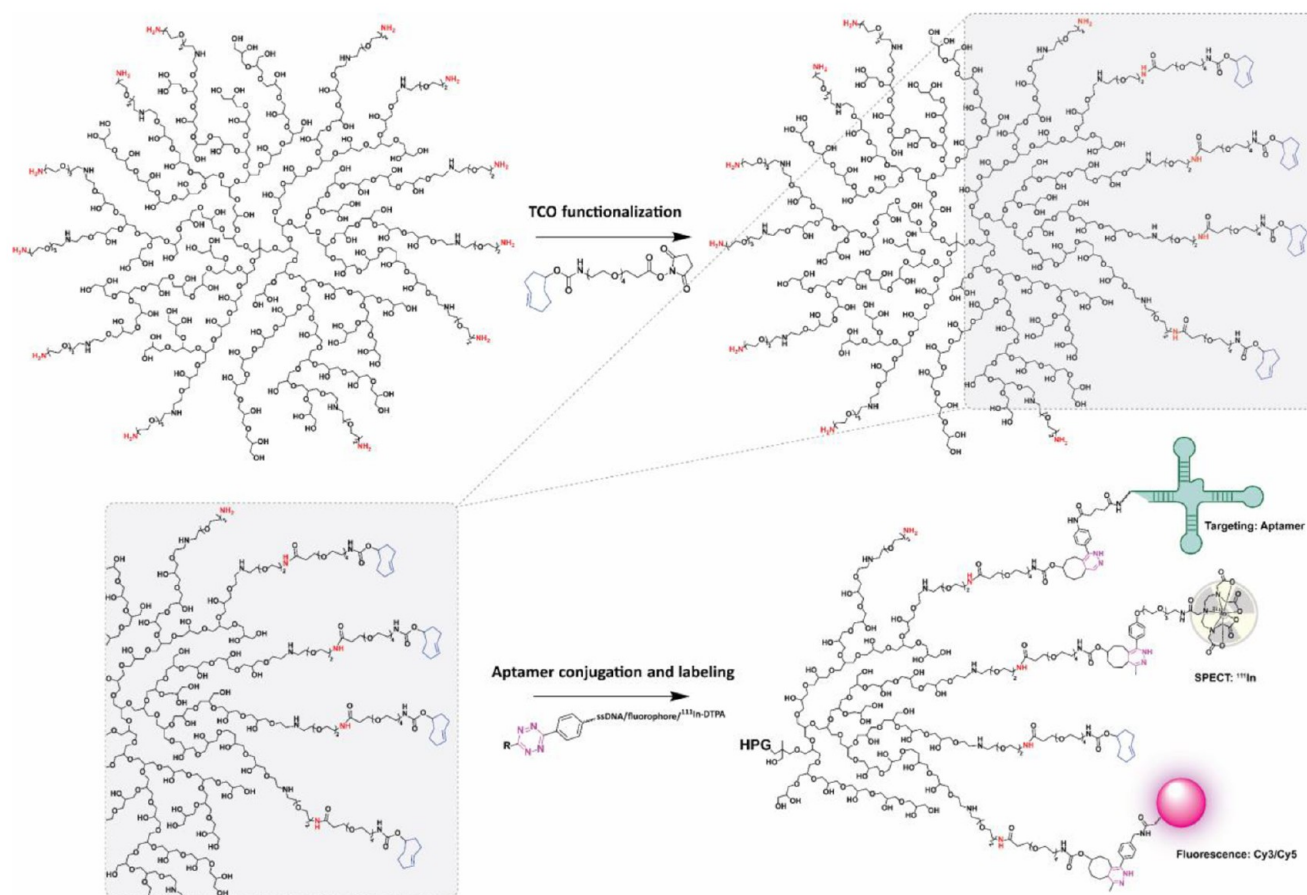One promising carrier is the polymer hyperbranched polyglycerol (HPG), a pseudodendrimer which can be readily

Scheme 1. Functionalization of HPG with TCO and Subsequent Conjugation of ssDNA (sgc8/scr), Fluorescent Dyes (Cy3/Cy5), and the Radioisotope ^{111}In[a]

[a]The primary amines on HPG are TCO-functionalized via activated ester conjugation with TCO-PEG$_4$-NHS. A variety of ssDNA, fluorescence, and ^{111}In-DTPA-modified tetrazines is clicked to HPG-TCO using IEDDA click chemistry to afford a targeted multimodal fluorescence and SPECT nanoprobe.

synthesized with high molecular weight (MW) and low polydispersity by ring-opening multibranching polymerization of glycidol.[5] HPG and its derivatives have been utilized in a vast range of biomedical applications such as drug delivery, surface modification, organ preservation, and imaging.[6] The circulation half-life of HPG increases in a size-dependent fashion, ranging from 17, 38, and 48 h for 50, 100, and 500 kDa, respectively.[7] We have previously investigated high molecular weight HPG as a blood pool imaging agent due to its long circulation and excellent biocompatibility.[8] Moreover, Gd^{3+}-labeled HPG demonstrated increased tumor accumulation due to the enhanced permeation and retention (EPR) effect, illustrating its suitability as an imaging agent.[9,10]

HPGs can be more specifically directed with aptamers, an often-described class of targeting agents. Aptamers are short single-stranded oligonucleotides that are able to bind to a variety of molecular targets. In recent years, aptamers have been increasingly used as targeting moieties for nanomaterials for diagnostic and therapeutic purposes.[11,12] One of the best described DNA aptamers is arguably sgc8, which was selected against CCRF-CEM cells using cell-SELEX.[13] Tyrosine-protein kinase-like 7 (PTK7), also known as colon carcinoma kinase 4 (CCK4), has been identified as the molecular target of sgc8.[14] PTK7 is a catalytically inactive kinase with aberrant expression

profile in a variety of cancer cells and tissues, including colon carcinoma,[15,16] melanoma,[17] acute myeloid leukemia,[18,19] and liposarcoma[20] and has been suggested as a prognostic marker for gastric cancer[21] and breast cancer.[22] Consequently, sgc8 and sgc8c, a truncated version of the aptamer, have been extensively employed for targeted imaging and therapy of lymphomas in preclinical studies.[23−33] Moreover, efforts to image and treat other solid tumors such as colon carcinoma,[34−39] cervical carcinoma,[40,41] breast cancer,[42] and melanoma[43] have further corroborated the applicability of sgc8 as a potential targeting moiety for a broad variety of tumors.

To follow the aptamer with spatiotemporal precision and unparalleled sensitivity, a commonly used molecular imaging modality is nuclear imaging.[44] The combination of single-photon emission computed tomography (SPECT) or positron emission tomography (PET) and computed tomography (CT) allows the simultaneous detection and quantification of a radiolabeled imaging probe within the context of an organism, providing both functional and anatomical information about the localization and biological fate of such probes. In contrast to nuclear imaging, fluorescence imaging is readily available with a plethora of well-established dyes at modest cost, rendering it especially useful for in vitro testing and preclinical applications.[45] The application of multimodal imaging probes
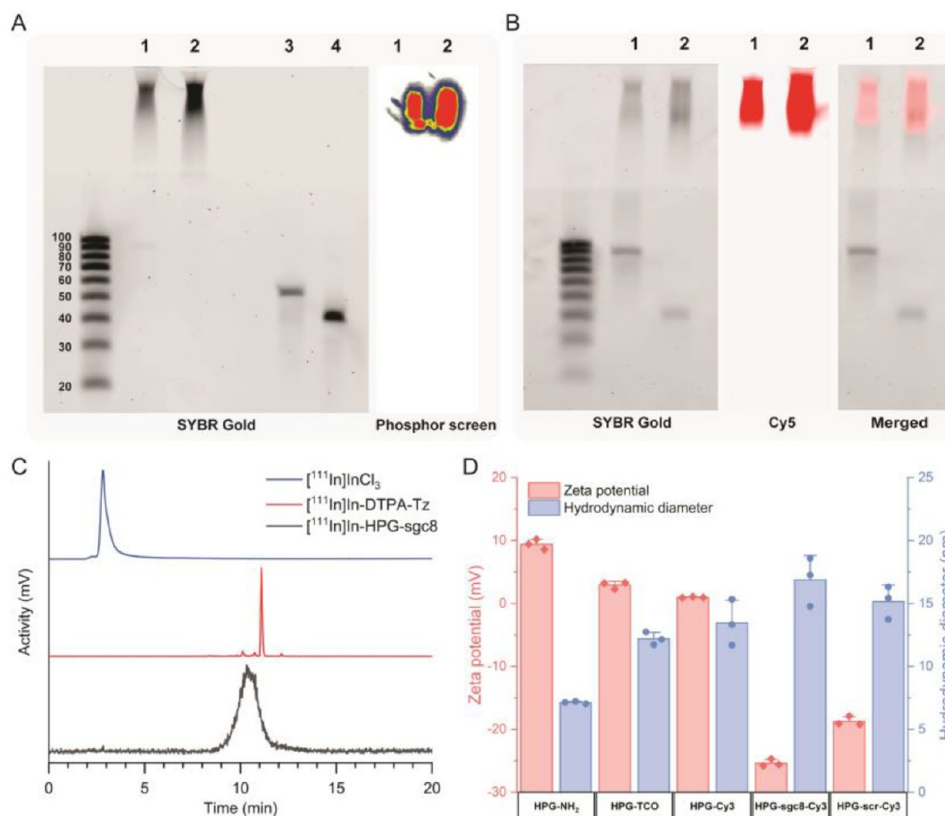
Figure 1. In vitro characterization of HPG-ssDNA constructs. (A) TBE-Urea gel electrophoresis of $[^{111}In]$In-HPG-sgc8 (1), $[^{111}In]$In-HPG-scr (2), NH$_2$-sgc8 (3), and NH$_2$-scr (4). SYBR Gold was used to stain ssDNA. The radioactive signal of ^{111}In was recorded on a phosphor imager. (B) TBE-Urea gel electrophoresis of HPG-sgc8-Cy5 (1) and HPG-scr-Cy5 (2). SYBR Gold was used to stain ssDNA; the red signal in the Cy5 channel corresponds to the fluorophore bound to HPG. (C) Radio-HPLC chromatograms of fresh $[^{111}In]$InCl$_3$ (blue), the labeled tetrazine prosthetic group $[^{111}In]$In-Tz-DTPA used for functionalization (red), and purified $[^{111}In]$In-HPG-sgc8 (black). (D) Hydrodynamic size and ζ potential of HPG-NH$_2$, HPG-TCO, HPG-Cy3, HPG-sgc8-Cy3, and HPG-scr-Cy3. Note that Cy3 was used to avoid interference with the laser of the DLS measurement. Conjugation of ssDNA leads to slightly increased size of the construct and a more negative ζ potential, corresponding to the negatively charged ssDNA.

which combine nuclear imaging capabilities for longitudinal studies with unlimited tissue penetration depth and fluorescence properties for in vitro and histochemical characterization thus allow harnessing these advantages in a single probe.[46]

To prepare multimodal imaging probes, click chemistry has since its inception in 2001[47] amassed tremendous interest for bioconjugation reactions by virtue of its ability to site-specifically functionalize (bio)molecules with virtually no side reactions and high yield under physiological conditions.[48,49] The inverse electron-demand Diels–Alder (IEDDA) reaction between 1,2,4,5-tetrazines and strained alkenes, most notably *trans*-cyclooctene (TCO), has been especially promising in this respect, due to its bio-orthogonality and rapid kinetics. This IEDDA reaction, followed by the irreversible loss of N$_2$ through a retro Diels–Alder reaction to form a stable cycloadduct, has also proven to be a powerful tool to radiolabel prosthetic groups of biomolecules under mild conditions.[50]

A considerable drawback of nonformulated aptamers is their susceptibility for nuclease degradation and rapid renal clearance.[51] Using a long-circulating carrier such as HPG could alleviate some of these shortcomings and allow for longer imaging times and higher tumor accumulation compared to free aptamers. Such an effect was observed for Evans Blue modified sgc8, which binds to human serum

albumin and in that way is markedly more nuclease resistant, and also shows better tumor retention.[36] To make the compound even more appropriate for drug delivery, a large polymer such as HPG can be used which contains many more functional groups than Evans Blue that can bind a large number of drug molecules.

In this study we evaluated the binding ability of aptamer-targeted and high molecular weight HPG to various cancer cell lines and used SPECT/CT imaging to investigate the in vivo tumor uptake in A431 xenograft bearing mice. Employing a versatile conjugation strategy based on the IEDDA reaction to covalently modify HPG with various functional groups, we combined the sensitivity and versatility of fluorescence for flow cytometry and confocal microscopy with the ability for quantitative deep tissue imaging of SPECT in a single multimodal probe. We further examined the toxicity of the probe in vitro and in vivo using confocal imaging and histology.

■ RESULTS AND DISCUSSION

Synthesis and Characterization of Functionalized HPG. A simple and versatile approach for modification of HPG was devised through the use of the IEDDA reaction between TCO-modified HPG and bifunctional tetrazines for targeting, radiometal chelation, and fluorescence (Scheme 1). To this end, amine-functionalized HPG with a MW of 800 kDa

was synthesized as described previously.[9] PEG$_4$-TCO-NHS was used to covalently modify HPG with a reactive TCO handle for subsequent functionalization through amide bond formation. The number of TCO moieties per HPG was determined to be 13.2 using NMR with a known concentration of a standard compound (Supporting Information Figure S1A), with 11.2 TCO molecules available for reaction determined by titration with fluorescently labeled tetrazine-Cy5 (Figure S1B). NH$_2$-modified sgc8 or scrambled control ssDNA was functionalized using 2-hydroxy-5-oxopyrrolidin-1-yl 5-((4-(1,2,4,5-tetrazin-3-yl)phenyl)amino)-5-oxopentanoate (Tz-NHS) and reacted with HPG-TCO to create aptamer-functionalized HPG (HPG-sgc8 and HPG-scr, respectively). For in vitro characterization, HPG-sgc8 and HPG-scr were further modified with tetrazine-Cy5 or tetrazine-Cy3. Successful coupling of ssDNA, fluorophores, and [^{111}In]In-DTPA was confirmed using gel electrophoresis. The large pseudodendrimer HPG is retained at the top of the gel while smaller ssDNA migrates further. Covalent conjugation of sgc8 and scr to HPG was confirmed using SYBR Gold nucleic acid stain, while the γ emission of ^{111}In colocalizes with HPG, indicating successful radiolabeling of HPG (Figure 1A). Similarly, the colocalization of ssDNA-modified HPG and Cy5 confirms covalent fluorescence labeling of the nanoprobe (Figure 1B). Tz-DTPA was labeled with ^{111}In with >95% radiochemical yield and used as a prosthetic group for labeling of HPG-TCO. Unreacted [^{111}In]In-Tz-DTPA was removed using Amicon Ultra centrifugal filters with a cutoff of 500 kDa to afford the fully functionalized HPG construct with >98% radiochemical purity (Figure 1C). For a typical reaction, each HPG molecule was modified with 2−3 fluorophores and 2−3 aptamers. The amount of [^{111}In]In-DTPA was negligible as only trace amounts of the radioisotope were needed for radiolabeling. Dynamic light scattering (DLS) was used to track the change in hydrodynamic size and surface potential of HPG over the course of the modification steps (Figure 1D). The hydrodynamic size of HPG-NH$_2$ increased from 7.14 to 12.2 nm after TCO functionalization. Subsequent functionalizations with Cy3 and scr or sgc8 were characterized by a further size increase to 13.45, 15.16, and 16.88 nm, respectively. Similarly, the slightly positive ζ potential of HPG-NH$_2$ decreased to −18.73 and −25.37 mV, respectively, after conjugation of scr or sgc8 due to the negatively charged phosphate backbone of the ssDNA.

Flow Cytometry Showing Broad Spectrum Affinity of sgc8 and HPG-sgc8 to Different Cancer Cell Lines. Previous studies with sgc8 showed a relatively broad specificity profile against a range of cancer cells that include A20,[30] MOLT-4,[13,52] HCT116,[36,37] Jurkat,[53] HeLa,[54,55] Caco-2,[56] MCF-7,[57] and A375 melanoma cells.[58] Most often, however, CCRF-CEM cells were used for in vitro and in vivo evaluation of sgc8-based probes against which the aptamer was originally selected.[59] Interestingly, we found moderate to strong binding of AlexaFluor647-labeled sgc8 against a number of pancreatic cancer derived BxPC-3, Capan-2, and MIA PaCa-2 cells (Figure 2). Binding was also observed against the metastatic breast cancer cell line MDA-MB-468 and the epidermoid carcinoma cell line A431, as well as human embryonic kidney derived HEK-293 cells (Figure 2), whereas no binding was observed for scr at the same concentration. These results suggest a relatively broad affinity that might allow sgc8 to be used in a variety of cancers. Despite being touted to be highly specific against their molecular targets, increasing evidence
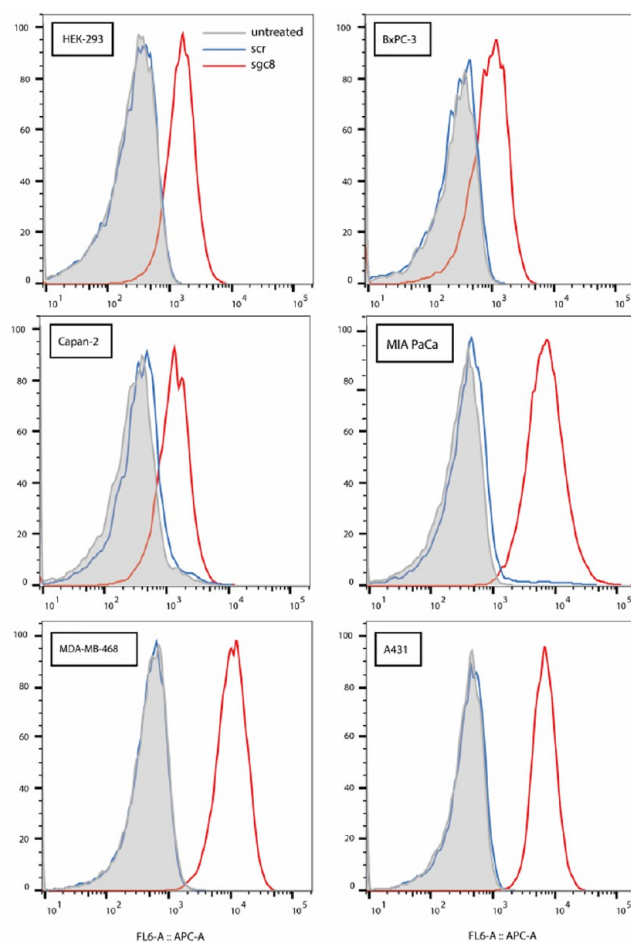

Figure 2. Binding of sgc8 aptamer to various cell lines. AlexaFluor647-labeled sgc8 was incubated with cells at a concentration of 5 nM. Strong binding was observed for MIA PaCa, MDA-MB-468, and A431 cells, while moderate binding was observed for HEK-293, BxPC-3, and Capan-2 cells. No binding was observed for a scrambled control sequence (AlexaFluor647-scr).

highlights the need for systematic evaluation of specificities of previously reported aptamers.[60−62] Possible reasons for this considerable problem are electrostatic interactions,[63] non-specific uptake by dead cells or target-independent uptake,[64−66] lack of target specificity,[67,68] systematic differences in binding assys,[69] and ubiquitously expressed molecular targets that complicate the search for truly specific binding sequences using cell-SELEX.[70] While most of these shortcomings can be mitigated by the use of precautinary measures and adequate controls in the experimental design, there is a lack of validation for many reported aptamer sequences. Sgc8 has been extensively used in previous studies and has indeed shown specific binding to PTK7.[60] Nonetheless, all flow cytometry experiments in the present investigation included LIVE/DEAD fixable violet staining to gate out dead cells, as well as nonspecific blocking using salmon sperm DNA. To evaluate whether the binding of sgc8 was indeed attributable to a specific interaction with the putative target PTK7, we performed competition experiments with unlabeled sgc8 (Figure S3). The addition of excess amounts of sgc8 prior to incubation with AlexaFluor647-sgc8 diminished binding, confirming specificity for target recognition.

Next, we evaluated whether HPG-conjugated sgc8 would retain binding affinity. Similar to free ssDNA, no binding was observed for HPG-scr (Figure 3A), while a concentration-
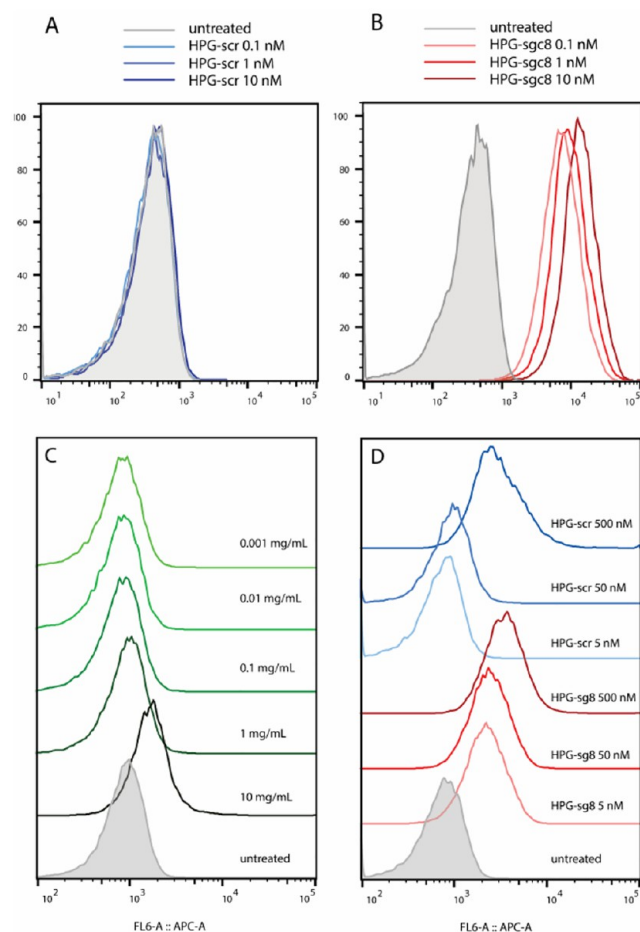

Figure 3. ssDNA-mediated specific binding of HPG against HEK-293 (A, B) and MDA-MB-468 cells (C, D). (A) No binding of HPG-scr at concentrations of 0.1 to 10 nM is observed. (B) Strong binding is observed for HPG-sgc8 even at low-nanomolar concentrations. (C) Nonfunctionalized HPG does not show nonspecific binding until high concentrations. (D) ssDNA-modified HPG shows specific binding for sgc8 even at low to moderate concentrations. Nonspecific binding of HPG-scr is observed only at a concentration of 500 nM.

dependent shift of fluorescence for HPG-sgc8 suggests that HPG is a suitable nanocarrier for this aptamer (Figure 3B). To rule out the possibility of HPG binding nonspecifically to cells, MDA-MB-468 cells were incubated with various concentrations of untargeted HPG-Cy5 (Figure 3C). Noticeable nonspecific binding was only observed at a concentration of HPG of 10 mg/mL, which is well above the typical concentration of ssDNA-modified HPG used in this study. This confirms that sgc8 is indeed conferring binding affinity when used as a targeting vector for HPG. The influence of ssDNA on binding was further evaluated over a broader concentration range of 5−500 nM (Figure 3D). While no binding of HPG-scr against MDA-MB-468 cells was observed at 5 and 50 nM relative ssDNA concentration, nonspecific binding at 500 nM scrambled ssDNA highlights a general propensity of ssDNA for nonspecific binding at higher concentrations.[71] Nevertheless, the strong binding of HPG-sgc8 at lower concentrations confirms the specific affinity of

the aptamer in the expected concentration range and corresponds well with a reported low-nanomolar affinity of sgc8 against CCRF-CEM cells[13] and ^{18}F-labeled sgc8 to HCT-116 cells[37] and a subnanomolar affinity of sgc8c to recombinant PTK7.[30]

A more comprehensive analysis of the binding profile of HPG-sgc8 was performed by investigating the influence of temperature on cell binding. Often times cell-SELEX is performed at 4 °C to prevent nonspecific uptake of aptamers at elevated temperatures.[13,72] A downside of this approach is that some aptamers selected at low temperatures might show reduced binding at physiological temperatures.[73] We detected minimal nonspecific binding of HPG-scr to A431 cells at 4 °C up to a concentration of 50 nM, while HPG-sgc8 exhibited maximum binding even at a concentration of 1 nM (Figure 4). This finding indicates specific interaction of HPG-sgc8 with PTK7 since energy-dependent HPG cell uptake should be minimized at this temperature. Over the same concentration range, a pronounced fluorescence shift of HPG-scr was observed at 37 °C, suggesting a non-negligible contribution of nonspecific, energy-dependent cell uptake of ssDNA-conjugated HPG (Figure 4). A possible reason for this observation is that, similar to reports of AS1411, total binding and cell uptake could be a combination of saturable specific interaction between sgc8 and PTK7 and a nonsaturable uptake mechanism for ssDNA at higher concentrations.[71] Uptake of HPG-Cy5 in A431 cells was evaluated in a similar fashion and showed negligible binding at 4 °C at a concentration of 0.001− 1 mg/mL and more pronounced uptake at 10 mg/mL. In contrast a clear concentration-dependent fluorescence shift of cells treated with HPG-Cy5 at 37 °C suggests a significant temperature-dependent uptake of not just ssDNA but also HPG (Figure S4). In order to test the binding of HPG-Cy5-sgc8 against a nonmalignant cell line that was expected to behave as nonbinding control cells, HUVEC cells were incubated with HPG-Cy5-sgc8 and HPG-Cy5-scr at 4° and 37 °C (Figure S5). Although binding of HPG-Cy5-sgc8 at 4 °C was lower than in A431 cells, concentration-dependent binding was clearly noticeable. Interestingly, less nonspecific uptake of HPG-Cy5-scr was observed at 37 °C, indicating a smaller contribution of the putative saturation-independent uptake mechanism in HUVEC cells.

Collectively, our findings suggest that sgc8 and in equal measure HPG-sgc8 appear to have a high affinity for the majority of tested cell lines, raising some questions regarding its reported specificity. Indeed, if the often corroborated claim of PTK7 specific binding holds true, binding to PTK7-negative cell lines should be absent or at the very least not exceed the innate moderate, nonspecific binding that is expected for ssDNA. However, Jacobsen et al. measured a K_d of 2.7 nM for ^{18}F-labeled sgc8 against PTK7-positive HCT116 cells, while PTK7-negative U87MG cells still showed a binding affinity of 16.9 nM.[37] Although a case for a correlation between PTK7 expression and binding affinity can be made for these results, it could be argued that PTK7, although demonstrably recognized by sgc8,[14] might not actually be the sole binding target. It is noteworthy that all tested cell lines are cancer-derived malignant cell lines that might share a ubiquitously expressed common target that contributes to the binding of sgc8. While we still could detect some binding to HUVEC cells, the mean fluorescence of HPG-Cy5-sgc8 treated A431 cells was 9.2- and 4.5-fold higher compared to HUVEC cells at a 1 nM concentration at 4 and 37 °C.
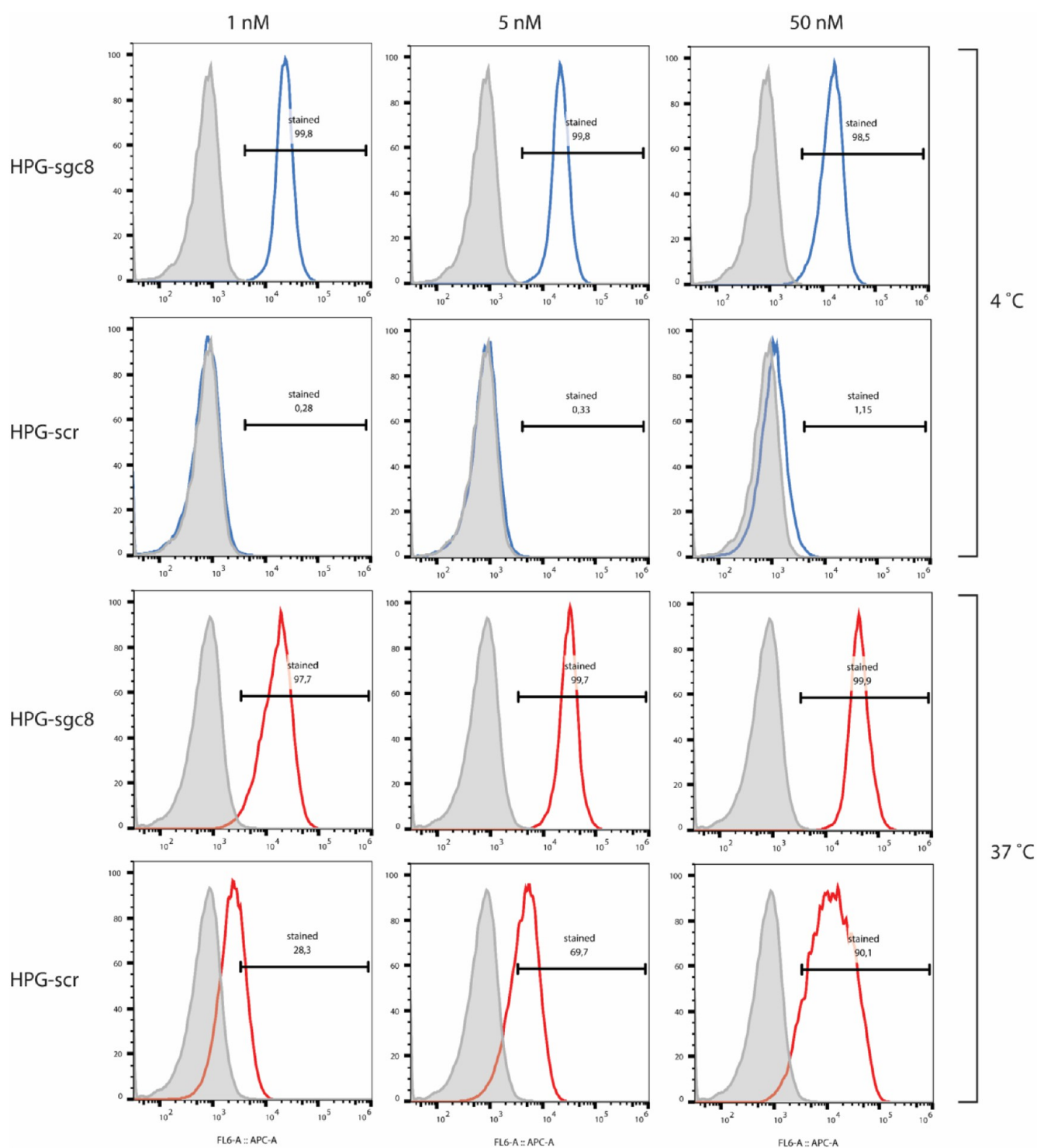
Figure 4. Effect of temperature on specific and nonspecific binding of HPG-ssDNA on A431 cells. At 4 °C, binding saturation of HPG-Cy5-sgc8 was reached at a concentration of 1 nM and did not increase further with higher concentrations. No binding was observed for HPG-Cy5-scr over the same concentration range. A similar profile for HPG-sgc8 was observed at 37 °C, while HPG-Cy5-scr showed considerable concentration-dependent uptake. Nontreated cells are shown in light gray; colored lines are cells treated with HPG-Cy5-sgc8 and HPG-Cy5-scr, respectively.

Confocal Microscopy and In Vitro Functionalization of HPG. Confocal imaging with HPG-Cy5-sgc8 confirmed the results of flow cytometry and showed specific binding to HEK-293, MDA-MB-468, and A431 cells, indicated by membrane localized fluorescence. In contrast, HPG-Cy5-scr did not lead to any membrane staining and only minor nonspecific cell uptake (Figure 5). The presence of TCO on our nanoprobe allowed us to utilize in vitro click chemistry to further evaluate if aptamer-targeted HPG binds to the extracellular side of the membrane as would be expected for PTK7-mediated binding. To this end, MDA-MB-468 cells were incubated with HPG-Cy5-sgc8 at 37 °C for 30 min followed by the addition of 50 μM tetrazine-Cy3. Confocal imaging showed predominant membrane staining for HPG-Cy5-sgc8 and some intracellular
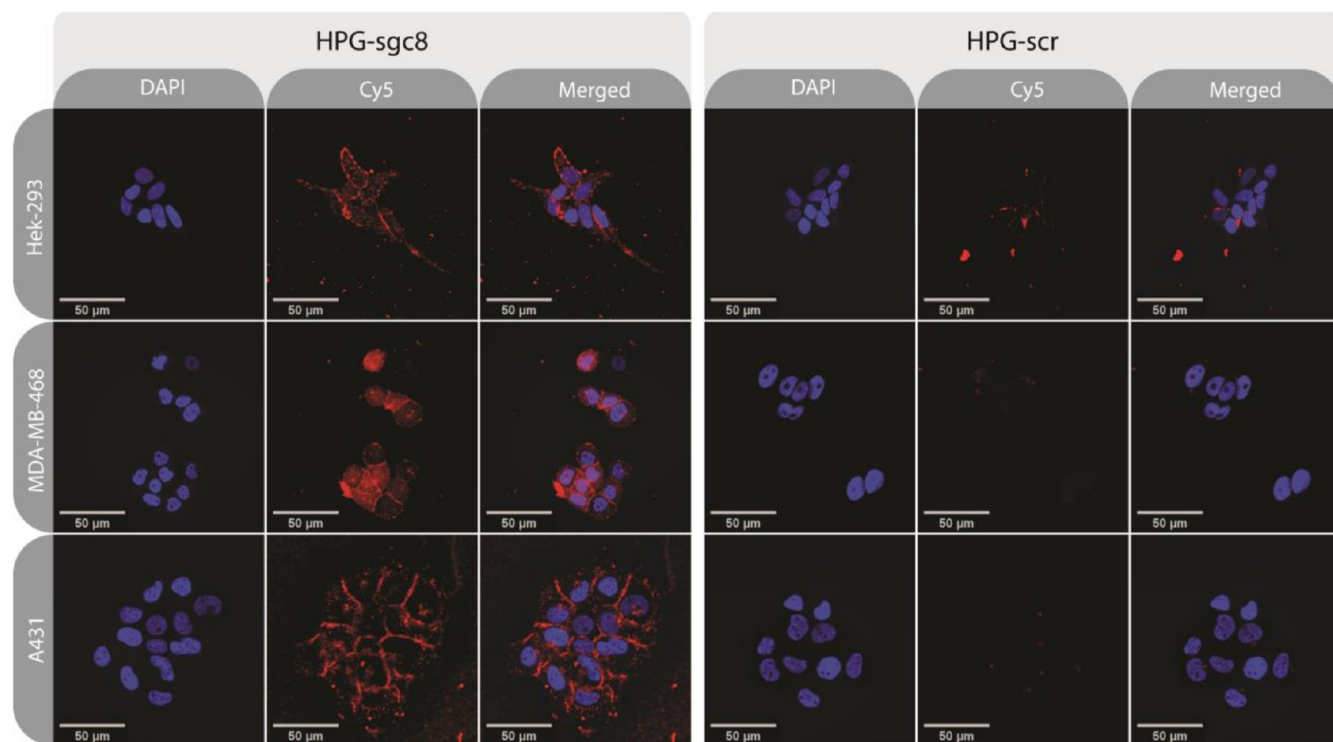
Figure 5. Confocal imaging of HPG-Cy5-sgc8 and HPG-Cy5-scr on HEK-293, MDA-MB-468 and A431 cells at 40× magnification. HPG-Cy5-sgc8 shows clear membrane localization with some diffuse intracellular uptake, especially in MDA-MB-468 cells. HPG-Cy5-scr does not bind to the cell membrane, and only weak intracellular uptake is visible. The scale bar in all pictures is 50 μm.

uptake, while the fluorescence signal of the tetrazine-Cy3 was mostly confined to colocalized staining of the extracellular membrane (Figure 6A). Membrane staining was absent in additional experiments with nonfluorescent HPG-scr co-incubated with Cy3-labeled tetrazine, confirming the specific interaction with extracellular PTK7 (Figure S6). Similar results were achieved by reacting the [^{111}In]In-Tz-DTPA prosthetic group with free TCO moieties of membrane-bound HPG-sgc8. A 2-fold increase of cell-bound radioactivity compared to untreated cells or cells incubated with HPG-scr was found (Figure 6C). Flow cytometry with fluorescently labeled sgc8 and HPG-sgc8 showed strong staining of cells even at low-nanomolar concentrations. Using radiolabeled HPG-sgc8, the binding affinity of the targeted nanoprobe against MDA-MB-468 cells was determined to be 4.02 ± 0.70 nM, which is lower than the reported K_d of 0.8 nM against CCRF-CEM cells[13] (Figure 6B). While differences might be attributable to varying PTK7 expression levels between different cell lines, the affinity is within the same order of magnitude and comparable to HCT116 cells.[37]

Biocompatibility and Stability of HPG-Conjugated Aptamers. Aptamers are generally well tolerated, and to this date, no toxicological or immunogenic properties beyond minor oligonucleotide class-based effects have been reported.[74] Similarly, HPG is well-tolerated in high doses in mice[75] and rats[76] and has been shown to be non-immunogenic.[77] Aminated HPG has further demonstrated low cytotoxicity and excellent blood compatibility.[78] The effect of aptamers on cell proliferation on HUVEC cells as well as of HPG-sgc8 and HPG-scr on HUVEC, MDA-MB-468, and HEK-293 cells was evaluated (Figure 7). Even at high concentrations of up to 4 μM sgc8 no detrimental effect on the growth of HUVEC cells could be detected. Similarly, HPG-sgc8 and HPG-scr up to a concentration of 500 nM did not influence cell viability or morphology (Figure S7).

Our rationale for using HPG-conjugated sgc8 was to counteract the fast clearance of aptamers in vivo, which allows imaging of the targeted nanoprobe over multiple days instead of minutes, as it is usually the case for unformulated aptamers. Due to their size of approximately 2 nm, aptamers are rapidly removed from circulation via renal filtration.[51] Metabolic degradation by nucleases further reduces the plasma half-life of aptamers to minutes.[79,80] Thus, we evaluated the plasma stability of free sgc8 and HPG-sgc8 in mouse plasma. The remaining ssDNA over time was fitted using a two-phase exponential decay function. With a plasma half-life of 16.03 ± 3.26 h, the stability of HPG-sgc8 was significantly increased compared to free sgc8 with a half-life of 4.87 ± 0.66 h (Figure 8).

In Vivo SPECT/CT Imaging of Radiolabeled HPG-Aptamer Probes. To evaluate the tumor targeting ability of HPG-Cy5-sgc8 in vivo, male CB-17 SCID mice bearing subcutaneous A431 xenografts were intravenously injected with the ^{111}In-labeled nanoprobe. Two control groups of tumor animals were injected with HPG-Cy5-scr and HPG-Cy5, respectively, to account for nonspecific uptake of ssDNA-modified HPG and EPR-mediated uptake of HPG.[7,9] Animals received approximately 1 mg of the respective nanoprobe corresponding to an activity of 9.28–10.09 MBq. SPECT/CT images for each mouse were acquired 10 min, 20 min, 3 h, 6 h, 24 h, and 48 h postinjection. Immediately following the last imaging time point, mice were sacrificed for an ex vivo biodistribution study. Figure 9A shows SPECT/CT images of a mouse after injection of [^{111}In]In-HPG-Cy5-sgc8. Representative images for [^{111}In]In-HPG-Cy5 and [^{111}In]In-HPG-Cy5-scr are shown in Figure S8A,B, respectively. Immediately
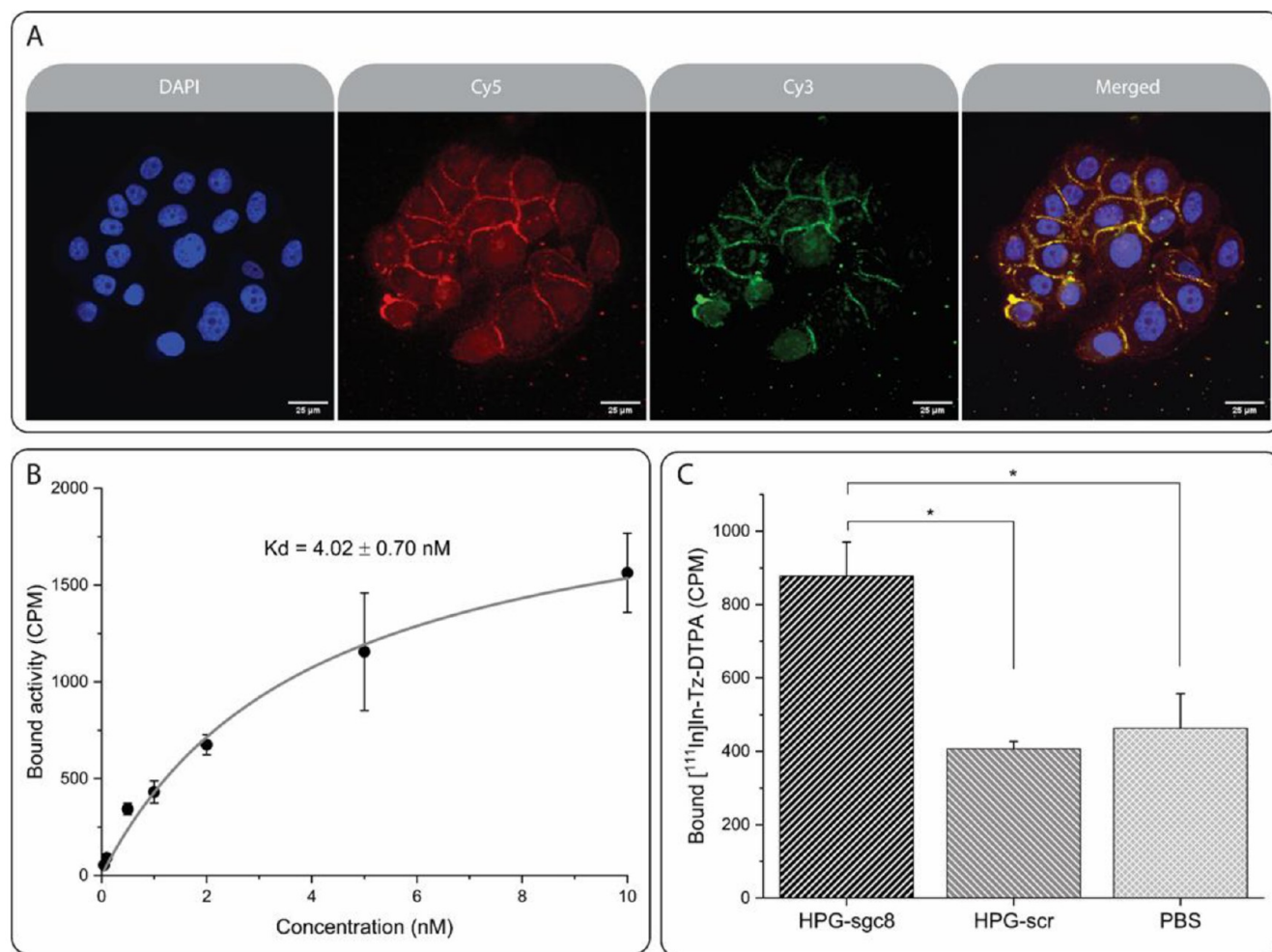
Figure 6. Cell binding of [111In]In-HPG-sgc8 and in vitro pretargeted labeling of HPG-sgc8 using tetrazine-Cy3 and the [111In]In prosthetic group. (A) MDA-MB-468 cells incubated with HPG-Cy5-sgc8. After 30 min tetrazine Cy3 was added before the cells were stained with fixing medium containing DAPI. Obvious membrane staining indicates binding of the nanoprobe to PTK7 on the cell surface; a more diffuse uptake points to some internalization. Tetrazine-Cy3 is only able to bind to free TCO groups on the membrane-bound HPG. The scale bar in the pictures is 25 μm. (B) Binding affinity of 111In-labeled HPG-sgc8 to MDA-MB-468 cells. (C) Cells preincubated with HPG-sgc8 showing a more than 2-fold increased binding of [111In]In-Tz-DTPA compared to cells treated with HPG-scr or PBS. Statistical significance (*, $p < 0.05$) was determined using Student's t test; $n = 3$.

following injection, high activity could be observed in heart, lungs, and major blood vessels for all formulations. As a long-circulating polymer, high molecular weight HPG has a long biological half-life with final uptake by the reticuloendothelial system and sustained residence in liver and spleen.[75] This is highlighted by a visible decrease in blood activity over time and pronounced liver uptake 24 and 48 h postinjection. The blood half-life for the different formulations was determined from the activity in the heart (Figure 9B) and showed comparable values of 19.7, 18.3, and 19.1 h for [111In]In-HPG-Cy5-sgc8, [111In]In-HPG-Cy5-scr, and [111In]In-HPG-Cy5, respectively. Quantitative analysis revealed a two-phase exponential decay kinetic for the liver with an initial rapid decrease with a half-life of 2.1−3.5 h followed by a prolonged period of slow excretion with a half-life of >300 h (Figure 9C). Due to the size of >10 nm for the high molecular weight HPG in this study, renal filtration is expected to be minimal. Activity in the bladder was visible only in the first minutes after injection, potentially corresponding to free 111In or [111In]In-Tz-DTPA. Interestingly, sustained activity levels were found in the renal cortex

(Figure 9D). A potential reason for this could be a slow release of 111In from the formulation due to kinetic instability of the DTPA chelator, which was expected from the measured slow in vitro release from HPG in plasma (Figure S10). Another contributing factor could be that HPG, while being small enough to extravasate through the fenestrated endothelium in the kidney, is too large to escape through the pores between podocytes and becomes entrapped in the glomerular basement membrane.[81] Tumor uptake was visible after 3 h and increased over the course of the study. Time−activity analysis of the highest intensity voxel in the tumor region revealed higher SUV_{max} levels for [111In]In-HPG-Cy5-sgc8 and [111In]In-HPG-Cy5 compared to [111In]In-HPG-Cy5-scr and little change over time. For a more robust measure of the activity concentration in the tumor, SUV_{95th} values were generated by quantifying the median of the top 10% hottest voxels in the tumor region.[82] No statistically significant difference in SUV_{95th} was observed between the three formulations (Figure 9E). [111In]In-HPG-Cy5-scr tumor accumulation reached 5.7 ± 4.2 and 6.7 ± 4.4% of the injected dose 24 and 48 h hours
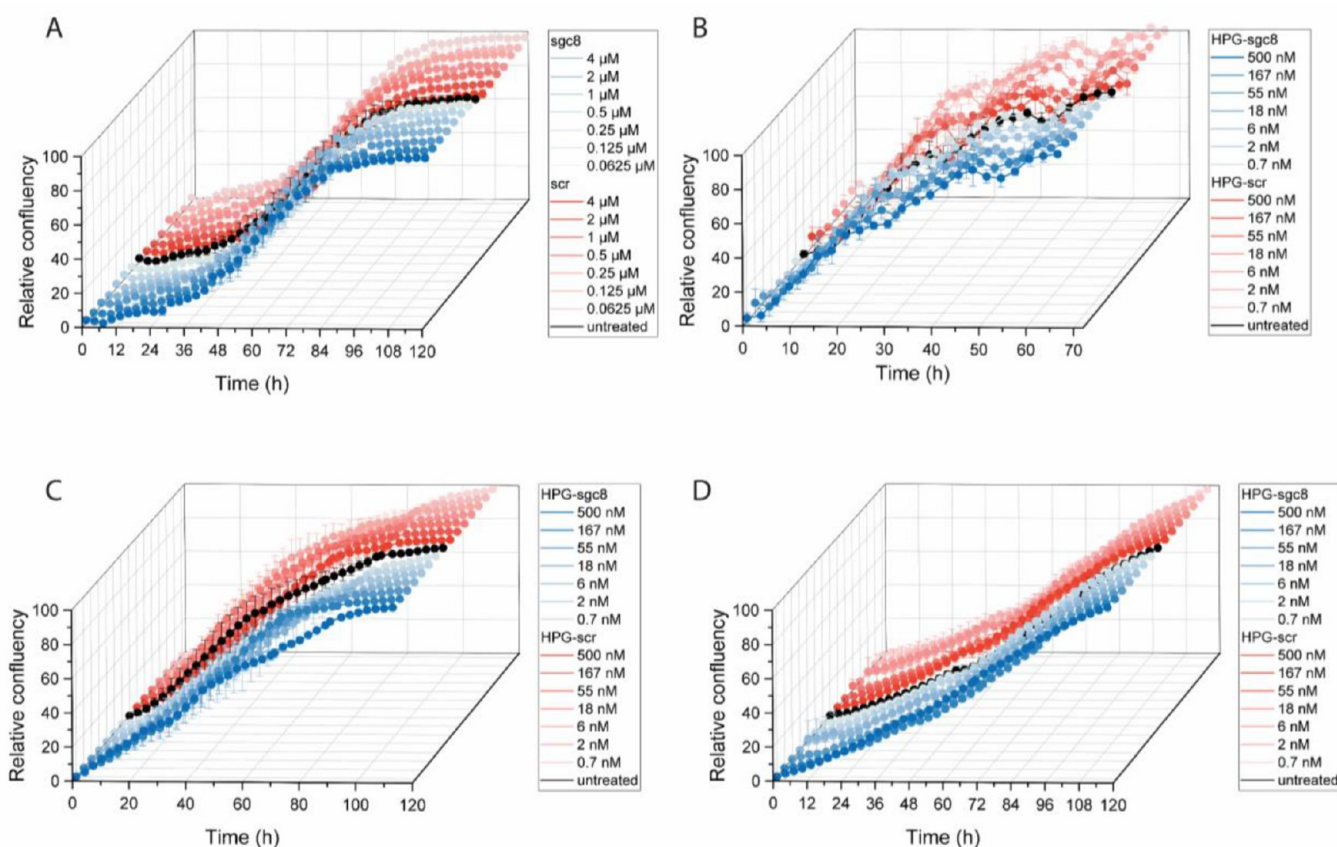
Figure 7. Cellular toxicity of aptamers and HPG functionalized with aptamers. (A) Proliferation of HUVEC cells in medium supplemented with free sgc8 or scr aptamer. No effect on growth of HUVEC (B), MDA-MB-468 (C), and HEK-293 (D) cells incubated with HPG-sgc8 and HPG-scr was observed.
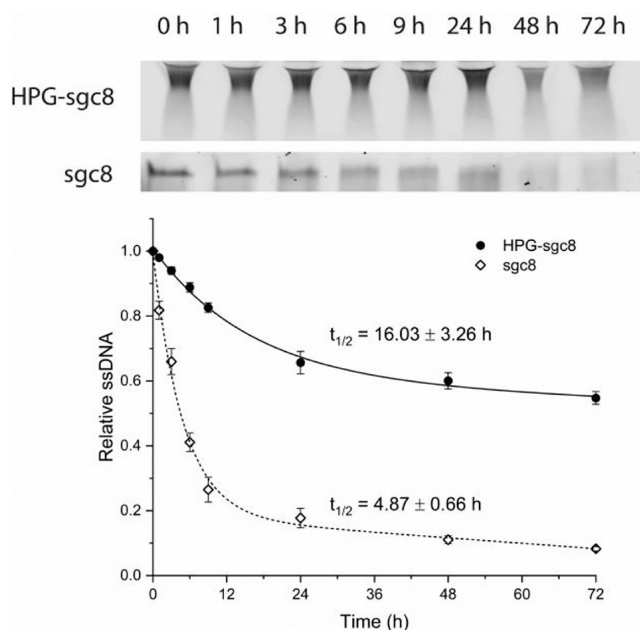

Figure 8. Stability of sgc8 and HPG-sgc8 in plasma. Sgc8 and HPG-sgc8 was incubated in fresh mouse plasma at 37 °C. At different time points aliquots were taken and analyzed using TBE-urea gel electrophoresis. DNA was visualized using SYBR Gold nucleic acid stain. The intensity was normalized to time 0 and fitted using a one-phase exponential decay function.

postinjection, respectively. Tumor uptake of [111In]In-HPG-Cy5-sgc8 and [111In]In-HPG-Cy5 was significantly higher at these times (12.1 ± 3.4, 14.8 ± 3.0% and 11.6 ± 2.7, 14.5 ± 3.2%, respectively). No statistically significant difference was observed between the tumor accumulation of [111In]In-HPG-Cy5-sgc8 and [111In]In-HPG-Cy5. The result of the ex vivo biodistribution showed comparable levels in all major organs between the different formulations and particularly high uptake in the liver (10.9 ± 0.8, 10.0 ± 0.5, and 12.5 ± 1.3% ID/organ for [111In]In-HPG-Cy5-sgc8, [111In]In-HPG-Cy5-scr, and [111In]In-HPG-Cy5, respectively). Maximum intensity projection (MIP) SPECT images showed inhomogeneous distribution of the formulations in the tumor (Figure S9). High uptake was found in the tumor periphery with low uptake in the core. Histopathology of paraffin embedded tumors showed large cystic cores in the tumor center surrounded by a dense peripheral region with poor perfusion (Figure 10A−D). The presence of Cy5 enabled us to further evaluate the distribution of the nanoformulations within the tumors and other organs. Tumor uptake was confined to the periphery of the tumor, and no uptake was found in the necrotic areas (Figure 10E,F). As expected from SPECT imaging and the biodistribution, liver and spleen showed strong uptake, characterized by homogeneous distribution of Cy5 fluorescence throughout these organs (Figure 10H,I). Heart, lungs, kidney, liver, and spleen appeared histologically normal in all three groups and showed no difference to untreated control animals, confirming the low toxicity for these formulations (Figure S11).
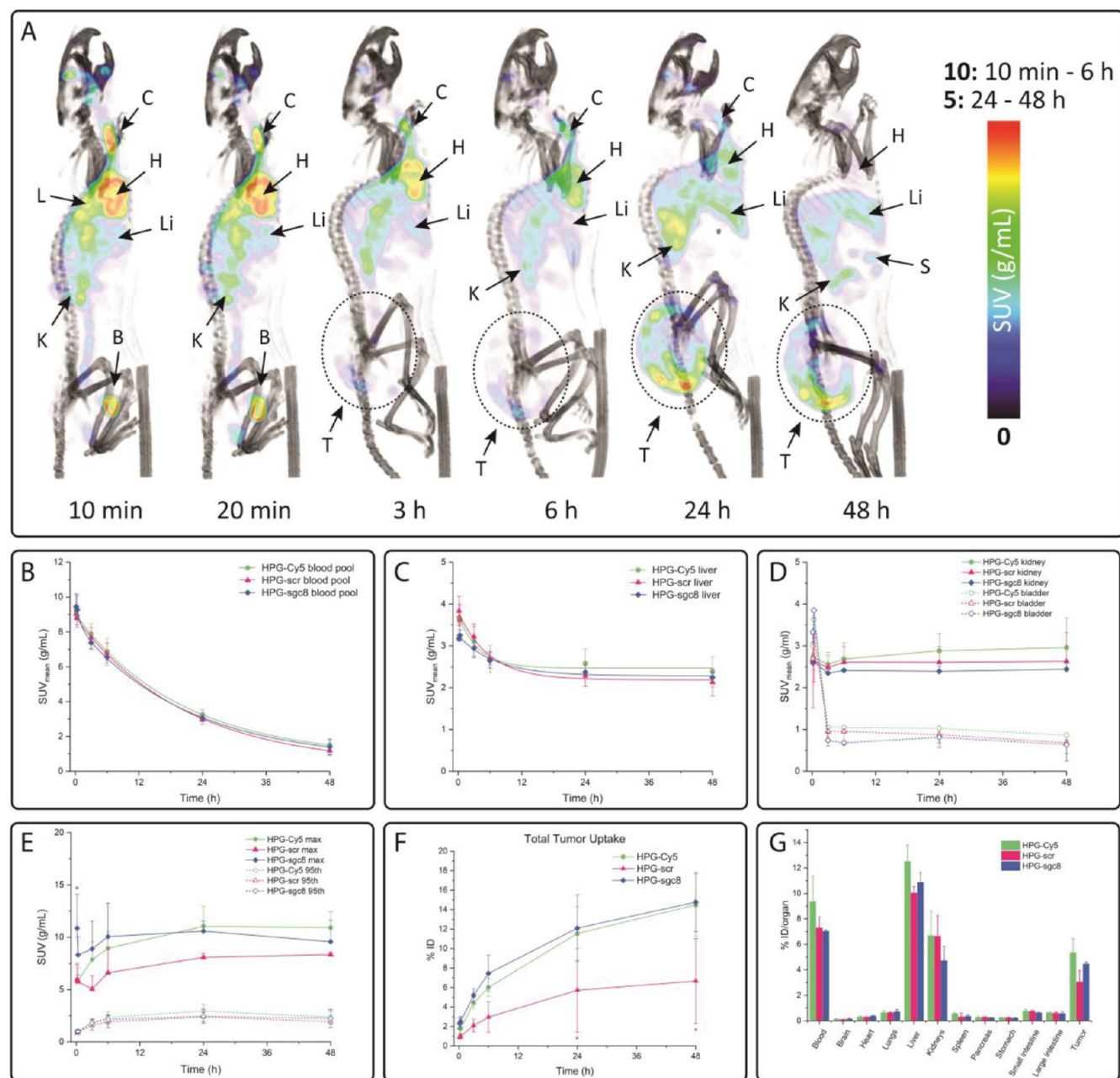
Figure 9. In vivo imaging of HPG-aptamer probes. (A) SPECT/CT MIP rendering of $[^{111}In]$In-HPG-Cy5-sgc8. Representative rendering of a mouse bearing a subcutaneous A431 tumor on the lower back. Initially high blood levels of the nanoprobe are visible, indicated by activity in carotid arteries, heart, and lungs. Liver uptake is evident at all time points but increases over time. Bladder activity is only visible at the earliest time points, although kidney levels remain relatively high throughout the study. Spleen uptake is visible after 48 h. CT in gray scale, SPECT in color. B, bladder; C, carotid artery; H, heart; K, kidney; L, lung; Li, liver; S, spleen; T, tumor area indicated by dashed circle. (B−D) Mean SUV in g/mL for blood pool, liver, kidney, and bladder. The majority of the activity for all formulations remained in the body; small amounts were excreted via renal and hepatobiliary elimination. (E) Comparison of SUV_{max} and SUV_{95th} in tumor region. $[^{111}In]$In-HPG-Cy5-scr shows consistently lower SUV_{max} in the tumor region, directly after injection, $[^{111}In]$In-HPG-Cy5-sgc8 shows a statistically significant higher SUV_{max} than the other formulations. (F) %ID in tumor region over time. $[^{111}In]$In-HPG-Cy5-scr shows a lower uptake than $[^{111}In]$In-HPG-Cy5-sgc8 and $[^{111}In]$In-HPG-Cy5. (G) Postmortem biodistribution (%ID/organ) at 48 h postinjection. Notable uptake was observed in blood, liver, kidneys, and tumors. Data represented as mean ± SD; $n = 3$. Statistical significance (*, $p < 0.05$) was determined using two-way repeated measurement ANOVA with a Holm−Sidak correction.

Contrary to our expectations and the in vitro results, no increased tumor uptake was observed for $[^{111}In]$In-HPG-Cy5-sgc8. In addition, we did not observe better retention of the aptamer-targeted probe in the tumor area compared to the control groups. While this failure to improve tumor accumulation or retention by the sgc8-targeted probe is disappointing, it supports the need for stringent controls and thorough analysis when using aptamers as targeting agents for nanoprobes. Quantitative SPECT analysis showed significantly lower SUV_{max} values and tumor uptake of $[^{111}In]$In-HPG-Cy5-scr compared to $[^{111}In]$In-HPG-Cy5-sgc8. The omission of a nonfunctionalized control might have erroneously concluded
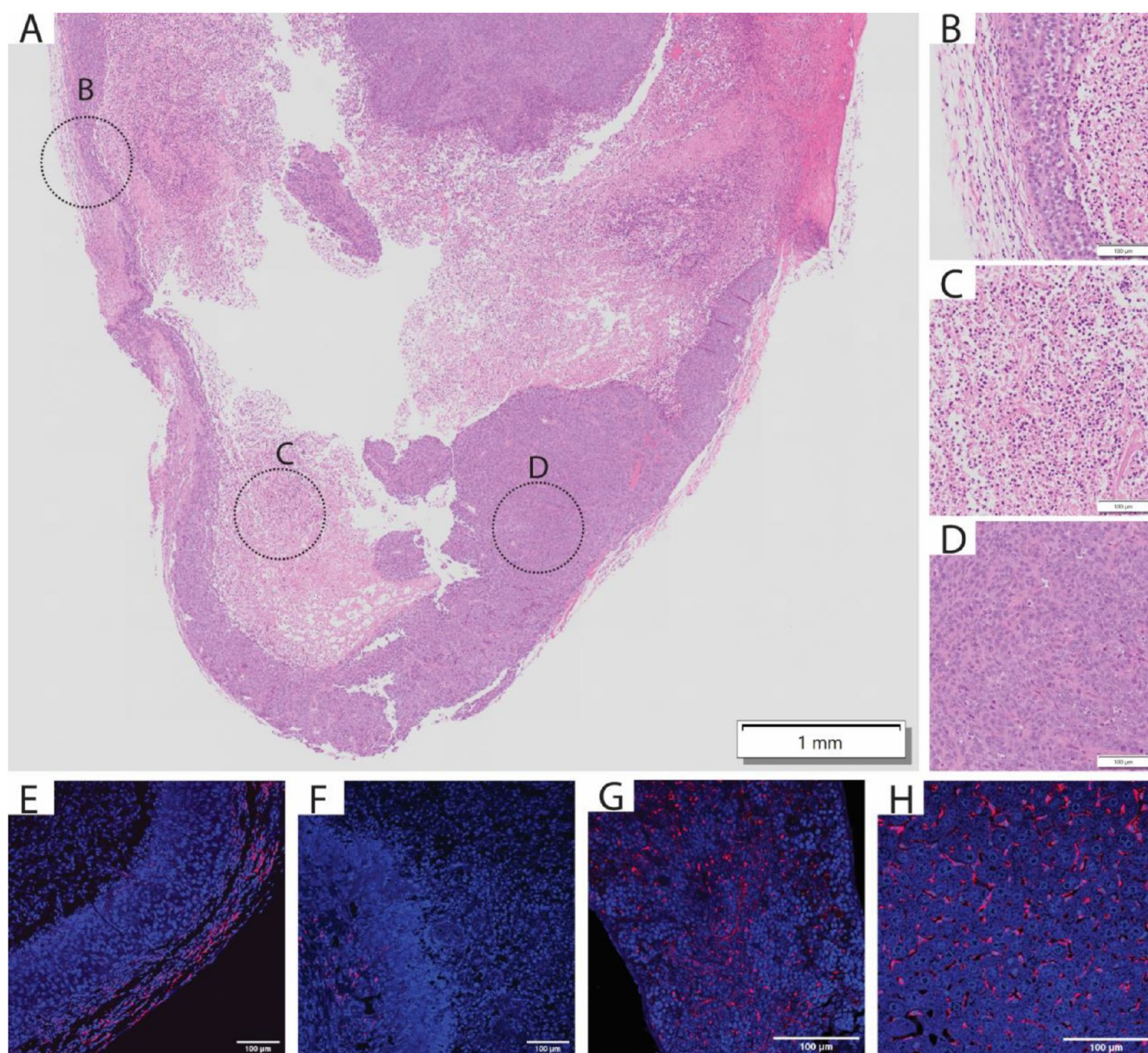
Figure 10. Representative tumor histology of HPG-Cy5-sgc8 injected mice. (A) Gross overview of A431 tumor. Large cystic core showing necrotic cells and void areas that were lost during sample preparation. Close ups of (B) tumor periphery, (C) necrotic area, and (D) central viable tumor region. Confocal images showing cell nuclei counterstained with DAPI in blue and the location of HPG-Cy5-sgc8 in red. (E) Majority of formulation found in the periphery of the tumor. (F) Very little fluorescence found in the core of the tumor. Spleen (G) and liver (H) showing high uptake of HPG-Cy5-sgc8, pointing to uptake by the reticuloendothelial system.

that sgc8 indeed leads to improved tumor uptake. The translation of promising in vitro results to functioning probes for in vivo imaging or therapy can be difficult and is not always guaranteed.[83,84] It should be noted that, to the best of our knowledge, hitherto no studies of sgc8 or sgc8-conjugated nanoprobes have been reported that target A431 xenografts. A variety of studies examined sgc8/sgc8c aptamers for therapy or imaging in vivo using a variety of cancer-derived cells such as CCRF-CEM,[23−29,32,33] A20,[30,31] HCT 116,[34−37,39] LS 174T,[38] HeLa,[40,41] and B16−F10.[43] Kelly et al. validated specific binding of sgc8c to A431 cells in vitro by knocking down PTK7 expression with siRNA.[60] While we clearly demonstrated in vitro binding, those results did not translate to the expected enhanced tumor uptake of [^{111}In]In-HPG-Cy5-sgc8

in vivo. A possible reason might be that A431 tumors are known to exhibit generally low and inhomogeneous tracer uptake, as shown by Sauter et al.[85] We observed large necrotic areas in all tumors, and the majority of the formulation in SPECT imaging and confocal microscopy was found in the periphery of the tumor. It is conceivable that other solid tumors with better perfusion might produce different results. Since we clearly observed EPR-mediated tumor uptake for all three formulations, a possible explanation for the lack of statistically significant differences could be attributed to a dominance of the EPR effect over active targeting.[86]

CONCLUSION

Key findings of this study include a wide specificity of sgc8 aptamer toward a range of cancer cells that have previously not been tested with this aptamer. We were able to readily prepare ssDNA-conjugated nanoformulations based on hyperbranched polyglycerol and successfully used click chemistry for efficient and versatile functionalization of the probes with fluorescent and radioactive reporter molecules. Excellent in vitro binding to various cell lines for sgc8-modified HPG was found by flow cytometry and confocal microscopy. However, a temperature-dependent uptake of HPG-scr in cells highlights innate challenges of ssDNA-targeted nanoprobes and should be considered in the development of such probes. Negligible cytotoxic effects against cells and excellent biocompatibility in vivo emphasize the broad applicability of HPG as a nanocarrier for diagnostic or therapeutic applications. In vivo, no improved tumor uptake of [^{111}In]InHPG-Cy5-sgc8 in A431 tumor animals over nontargeted HPG or HPG-conjugated to nonspecific control ssDNA was found. This finding highlights the necessity of stringent controls in the evaluation of aptamers as theranostic agents and serves as a reminder that extrapolations from in vitro reports of aptamer-targeted probes should be interpreted with caution with regard to in vivo translation. Improved tumor uptake with aptamer-targeted nanoformulations has indeed shown positive results.[36,87] A further evaluation of other tumor models for sgc8-targeted formulations is therefore warranted to explore the range of possible malignancies that can be targeted with this aptamer. HPG proved to be an excellent carrier for aptamers, offering protection from nuclease degradation and extended biological half-life which could improve the poor pharmacokinetics of aptamers. Further evaluation of the long-circulating polymer platform technology with a variety of other aptamers and tumor models might answer whether improved tumor delivery over purely EPR-mediated uptake can be achieved with this formulation.

MATERIALS AND METHODS

General Methods. All chemicals were purchased from Sigma-Aldrich (St. Louis, MO, USA), unless otherwise noted. [^{111}In]InCl$_3$ was purchased from BWXT (Peterborough, ON, Canada). Phosphate buffered saline (PBS), Hank's balanced salt solution (HBSS), Eagle's minimum essential medium (EMEM), Dulbecco's modified Eagle's medium (DMEM), Roswell Park Memorial Institute (RPMI) 1640, McCoy's 5a medium, penicillin/streptomycin (10,000 U/mL), 0.25% (w/v) trypsin-ethylenediaminetetraacetic acid (EDTA), cell lysis buffer, LIVE/DEAD fixable violet dead cell stain, SYBR Gold nucleic acid gel stain, Quant-iT OliGreen ssDNA assay kit, sheared salmon sperm DNA, and ProLong Diamond antifade mountant with DAPI were purchased from Thermo Fisher Scientific (Waltham, MA, USA). Cell culture flasks and 6- or 96-well plates were purchased from Sarstedt (Nümbrecht, Germany) or Corning (Corning, NY, USA). Sulfo-Cy3-tetrazine (CAS Reg. No. 1801924-47-9), sulfo-Cy5-methylte-trazine (CAS Reg. No. 1801924-45-8), and TCO-PEG$_4$-NHS ester (CAS Reg. No. 1613439-69-2) were purchased from BroadPharm (San Diego, CA, USA). Amicon Ultra centrifugal filter units with 10 and 500 kDa molecular weight cutoffs (MWCOs) were purchased from MilliporeSigma (Burlington, MA, USA). The tetrazine-DTPA was custom-made by Macrocyclics (Plano, TX, USA).

^{1}H NMR spectra were recorded on a Bruker Ascend-400 (Billerica, MA, USA) at 400.13 MHz and analyzed using MNova (Mestrelab Research, Santiago de Compostela, Spain). Graphing and curve fitting were preformed using Origin 2019 software (OriginLab, Northampton, MA, USA). Multipanel figures were prepared using Adobe Illustrator CC (Adobe, San Jose, CA, USA).

All HPLC-purified DNA sequences, as well as DNA ladders for gel electrophoresis, were synthesized from Integrated DNA Technologies (Coralville, IA, USA) and used without further purification. NH_2-sgc8: 5′-$\underline{NH_2}$-C$_{12}$H$_{24}$-ATA CCA GCT TAT TCA ATT AGT CAC ACT TAG AGT TCT AAC TGC TGC GCC GCC GGG AAA ATA CTG TAC GGT TAG ATA GTA AGT GCA ATC T-3′. *AlexaFluor647-sgc8*: 5′-$\underline{Alexa-Fluor647}$-ATA CCA GCT TAT TCA ATT AGT CAC ACT TAG AGT TCT AAC TGC TGC GCC GCC GGG AAA ATA CTG TAC GGT TAG ATA GTA AGT GCA ATC T-3′. NH_2-scr: 5′-$\underline{NH_2}$-C$_{12}$H$_{24}$-GAT CTA ACG CAG ACG CGA CCT ACG AAC TAC GGA CTA CTG A-3′. *AlexaFluor647-scr*: 5′-$\underline{AlexaFluor647}$- GAT CTA ACG CAG ACG CGA CCT ACG AAC TAC GGA CTA CTG A-3′.

Synthesis of 2-Hydroxy-5-oxopyrrolidin-1-yl 5-((4-(1,2,4,5-Tetrazin-3-yl)phenyl)amino)-5-oxopentanoate (Tz-NHS). Established literature protocols were used for the synthesis of the precursor 5-((4-(1,2,4,5-tetrazin-3-yl)phenyl)-amino)-5-oxopentanoic acid.[88,89] To functionalize the tetrazine with *N*-hydroxisuccinimide for modification of NH$_2$-sgc8 and NH$_2$-scr, 5-((4-(1,2,4,5-tetrazin-3-yl)phenyl)amino)-5-oxo-pentanoic acid (39 mg, 0.14 mmol), *N*-hydroxysuccinimide (NHS) (50 mg, 0.43 mmol), and 1-ethyl-3-(3-(dimethylamino)propyl)carbodiimide (EDC) were added to a dried microwave vial. A 1 mL aliquot of anhydrous DMF was added, and the solution was stirred for 18 h at room temperature. Water was added to the reaction mix until the product precipitated. The suspension was centrifuged (14000 RCF, 10 min), and the supernatant was decanted. The product was subjected to two more cycles of resuspension and centrifugation and dried under vacuum to yield the title compound as a pink solid (25 mg, 46% yield). ^{1}H NMR (400 MHz, DMSO-d_6): δ 10.52 (s, 1H); 10.38 (s, 1H); 8.47 (s, 2H); 7.90 (s, 2H); 2.83 (s, 4H); 2.79 (t, 2H); 2.54 (t, 2H); 1.97 (p, 2H) ppm.

Tetrazine Modification of NH$_2$-ssDNA. A 20 nmol amount of NH$_2$-sgc8 or NH$_2$-scr in ultrapure water (200 μL) was mixed with 2 mmol of Tz-NHS in anhydrous DMSO (80 μL) and 20 μL of 1 M sodium borate buffer, pH 8.2, and reacted overnight. The solution was diluted with ultrapure water to allow for purification with Amicon Ultra centrifugal filters with a 10 kDa MWCO to afford Tz-sgc8 and Tz-scr.

Radiolabeling of Tz-DTPA. A 1−3 μL aliquot of [^{111}In]InCl$_3$ in 0.1 M HCl with varying activity was reacted with 38 μg of Tz-DTPA in 1 μL of water in 8 μL of 0.1 M ammonium acetate buffer, pH 4.8, under shaking at 21 °C for 30 min. A CRC-55tR dose calibrator (Capintec, Flowham Park, NJ, USA) was used to measure the activity of all radioactive samples. Radiochemical conversion was monitored using analytical radio-HPLC chromatography on a Waters (Milford, MA, USA) Alliance e2695 separations module coupled to a Waters 2489 UV/vis detector and a Scan-RAM radio-TLC and HPLC detector (LabLogic, Sheffield, U.K.) installed with a Waters Atlantis T3 column (C18, 4.6 mm × 150 mm) and a Waters Atlantis T3 Sentry Guard Cartridge (C18, 2.1 mm × 10 mm). Solvent A, H$_2$O + 0.1% TFA;

Solvent B, 9:1 MeCN-H$_2$O + 0.1% TFA. Gradient: 0−3 min, 95% solvent A; 3−18 min, ramp to 100% solvent B; 18−23 min, 100% solvent B; flow, 1 mL/min. Radiolabeling proceeded with >95% radiochemical conversion (RCC), and [^{111}In]In-Tz-DTPA was used for labeling of HPG-TCO without further purification.

Synthesis of HPG-NH$_2$. Amine-modified HPG was synthesized according to previously published procedures.[9] Briefly, hydroxyl groups on HPG were oxidized to aldehyde and then coupled to 100 equiv of Boc-NH-PEG$_2$-NH$_2$ using reductive amination. Following deprotection, HPG-NH$_2$ was characterized using NMR and DLS.

Synthesis of HPG-TCO. To modify HPG-NH$_2$ with TCO for subsequent functionalization, HPG-NH$_2$ was reacted with 150 equiv of TCO-Peg$_4$-NHS in 0.1 M sodium borate buffer, pH 8.2. Excess TCO was removed by washing with ultrapure water with Amicon Ultra centrifugal filters with a 500 kDa MWCO.

Functionalization of HPG-TCO. *Aptamer Conjugation.* Tz-sgc8 and Tz-scr were reacted with HPG-TCO in 3-fold excess and purified in 10 washes with Amicon Ultra centrifugal filters with a 500 kDa MWCO to remove any nonspecifically adsorbed ssDNA. The amount of ssDNA conjugated to HPG was quantified using a Quant-iT OliGreen ssDNA assay kit from Thermo Fisher (Waltham, MA, USA) and analyzed on a SynergyMx plate reader (BioTek, Winooski, VT, USA). *Fluorescence Labeling:* HPG-sgc8 and HPG-scr were reacted with 3 equiv of Tz-Cy3 or Tz-Cy5 under shaking at 21 °C for 1 h. Any nonreactive fluorophores were removed by washing with ultrapure water with Amicon Ultra centrifugal filter units with a 500 kDa MWCO. *Radiolabeling:* HPG-sgc8-sgc8 and HPG-Cy5-scr were reacted with [^{111}In]In-Tz-DTPA under shaking at 21 °C for 1 h and purified using Amicon Ultra centrifugal filter units with a cutoff of 500 kDa. RCC of the labeling reaction was >90%, and the product had a radiochemical purity of >98%. Radiochemical purity of the HPG formulations was assessed using analytical radio-HPLC (vide supra) and instant-thin-layer chromatography (ITLC) with a TEC-Control 150-771 stationary phase from Biodex Medical systems (Shirley, NY, USA) and 0.1 M EDTA as mobile phase. ITLC strips were analyzed using a Cyclone phosphorimager and Optiquant software from Packard Instruments (Downers Grove, IL, USA). For the assessment of the radiochemical stability, ^{111}In-labeled HPG was incubated in fresh mouse plasma. At different time points, aliquots were taken and analyzed by ITLC in duplicate. The percentages of activity at the origin of the ITLC strip ($R_f = 0$) and at $R_f = 1$, corresponding to [^{111}In]In-HPG and noncomplexed ^{111}In, respectively, were quantified to determine the release of ^{111}In from the formulation over time.

Characterization of HPG-Aptamer Formulations. Hydrodynamic size and ζ potential were measured using dynamic light scattering on a ZetaSizer (Malvern Panalytical; Malvern, U.K.). TBE-Urea gel electrophoresis[90] was performed with two-phase gels with 6 and 15% acrylamide at the top and bottom halves, respectively. Reagents and materials for gel electrophoresis were purchased from Bio-Rad (Hercules, CA, USA). ssDNA was visualized with SYBR Gold nucleic acid stain and gels were imaged using a Sapphire Biomolecular Imager (Azure Biosystems, Dublin, CA, USA). The binding affinity of [^{111}In]In-HPG-sgc8 was determined by preparing MDA-MB-469 cells as described under general cell culturing methods. After incubation with [^{111}In]In-HPG-sgc8 at 37 °C

cells were washed thrice with binding buffer, and the amount of activity bound to the cells was determined on a calibrated Cobra II Autogamma counter (Packard Instruments). A saturation binding curve to determine the K_d was fitted in Origin 2019 (OriginLabs). To investigate the pretargeted binding of [^{111}In]In-Tz-DTPA, to HPG-sgc8 and HPG-scr, cells were grown in 96-well plates and incubated with either formulation at a concentration of 50 nM or PBS as control for 30 min at 37 °C. 1.1 MBq of of [^{111}In]In-Tz-DTPA was added per well and allowed to react for 20 min. Cells were washed thrice with 200 μL of binding buffer and harvested using cell lysis buffer, and the activity of the cell-bound activity was quantified on a Cobra II Autogamma counter.

Cell Lines and Cell Culture. HEK-293, BxPC-3, Capan-2, and MIA PaCa-2 cells were purchased from American Type Culture Collection (ATCC) (Manassas, VA, USA). MDA-MB-468 were kindly provided by Dr. Karla Williams, Faculty of Pharmaceutical Sciences, University of British Columbia and A431/H9 cells by Dr. Raffit Hassan at the National Institutes of Health (NIH). All cells were cultured in their respective ATCC recommended medium, supplemented with 10% FBS and 100 U/mL penicillin/streptomycin at 37 °C and 5% CO$_2$ atmosphere. HUVEC cells and endothelial growth medium-2 (EGM-2) were purchased from Lonza (Basel, Switzerland). For the assessment of cellular toxicity, cells were plated at a density of 5000 cells per well in a 96-well plate and incubated with increasing concentrations of aptamers and HPG formulations in culture medium. Growth kinetics and appearance over time were recorded on an Incucyte ZOOM live cell imager (Sartorius; Göttingen, Germany) and analyzed using the built-in software.

Flow Cytometry. Cells were grown to 80−90% confluency in T-25 or T-75 culture flasks and harvested using trypsin-EDTA. After resuspension in fresh medium, cells were allowed to regenerate for 1 h in 37 °C under 5% CO$_2$ atmosphere. After pelleting, cells were resuspended in 3 mL of binding buffer (sheared salmon sperm DNA (100 μg/mL), bovine serum albumin (1 mg/mL) in HBSS), and the concentration of the cells was determined using Trypan blue and a hemocytometer. Cells were aliquoted in vials of 250000 cells. Aptamers or HPG-aptamer formulations were added to the cells in the desired concentration in a final volume of 200 μL in binding buffer. Cells were then incubated for 30 min under gentle shaking at 37 °C, unless otherwise specified. Cells were subjected to a total of 3 washes with binding buffer and incubated for 5 min with a solution of LIVE/DEAD Fixable Violet Dead Cell Stain at a concentration of 1 μg/mL in binding buffer before the final washing step. 20000−30000 events per sample were recorded on a CytoFLEX cytometer (Beckman Coulter, Brea, CA, USA) and analyzed using FlowJo 10.8.1 software from BD (Franklin Lakes, NJ, USA).

Confocal Imaging. Cells were harvested following the same protocol as that for flow cytometry and seeded on 15 mm round coverslips that were previously coated with poly-D-lysine solution (Sigma-Aldrich) according to the manufacturer's instructions, at the bottom of a 6-well plate. When cells reached a confluency of 30−50%, solutions of aptamers or HPG-aptamers at a concentration of 10 nM in binding buffer were added to the wells and incubated for 30 min at 37 °C. The cells were washed 3 times with binding buffer and mounted on coverslips using ProLong Diamond antifade mountant with DAPI. Imaging was performed on a Zeiss LSM 700 laser scanning confocal microscope (Zeiss AG; Oberko-

chen, Germany) equipped with a 20× objective and a 43× oil objective. The laser lines for the different fluorophores were 405, 555, and 639 nm for DAPI, Cy3, and Cy5, respectively. For pretargeted staining of cells with Tz-Cy3, cells were plated as described previously. HPG-Cy5-Sc8 was added at a concentration of 10 nM in binding buffer and incubated for 30 min at 37 °C. After washing the cells thrice with binding buffer, 50 μM Tz-Cy3 was added and allowed to react for 20 min. Cells were then washed and mounted as described previously.

Aptamer Stability. For the assessment of aptamer stability, 0.65 μg of NH$_2$-sgc8 or HPG-sgc8 (relative ssDNA amount) in sterile PBS was incubated in fresh mouse plasma in a ratio of 1:2 at 37 °C in triplicate. At different time points 10 μL aliquots were taken and the ssDNA was recovered using methanol/chloroform extraction. Briefly, aliquots were mixed with 50 μL of PBS, 100 μL of MeOH, and 50 μL of CHCl$_3$ and lightly vortexed. Then 50 μL of water and 50 μL of CHCl$_3$ were added, and the sample was vortexed again before centrifugation at 500 RCF for 20 min. A 75 μL aliquot of the aqueous phase was collected and lyophilized to concentrate the ssDNA. Samples were redissolved, mixed with nucleic acid sample buffer, and separated on TBE-Urea gels as described previously. The DNA bands were quantified using Image Studio Lite (Li-COR Biosciences; Lincoln, NE, USA) and normalized to time point $t = 0$ h. A two-phase exponential decay function was fitted to determine the stability over time.

In Vivo SPECT/CT Imaging and Biodistributions. In vivo studies were conducted in accordance with the Canadian Council on Animal Care (CCAC) under protocol A20-0132, approved by the Animal Care Committee (ACC) of the University of British Columbia. Sixteen-week-old male CB-17 SCID mice were purchased from Taconic (Germantown, NY, USA). *Induction of Tumor Xenograft Models*: A431 cells were cultured to 80−90% confluency and harvested as described previously. Cells were pelleted and washed 3 times with PBS and stored on ice until injection. Mice were anesthetized using isoflurane, and 1×10^6 cells in a volume of 100 μL were injected subcutaneously into the lower back. Tumors were allowed to grow for 3−4 weeks and measured using calipers until tumors reached a size of 500−1000 mm^3. Tumor size was calculated as volume (mm^3) = $\frac{1}{2}$ × length (mm) × width^2 (mm^2). Animal weight and general health were monitored at least twice per week after injection of tumor cells and every second day once tumors were palpable. Animals were sacrificed when humane end points were reached. *In Vivo SPECT/CT Imaging*: Mice were randomly divided into 3 groups of 3 animals each. After induction of anesthesia with isoflurane (5% for induction, 1−2% for maintenance), on a RC2 rodent precision vaporizer (VetEquip; Pleasanton, CA, USA), an injection of 100 μL of the HPG formulation, at a concentration of 1 mg/mL (9.28−10.09 MBq), was administered via the tail vein. Immediately after injection, whole-body SPECT/CT scans were acquired at different time points (10 min, 20 min, 3 h, 6 h, 24 h, and 48 h). Throughout the imaging procedures, mice were kept under anesthesia and received heat support from an integrated heating source in the scanner bed. Body temperature and respiratory rate were monitored using BioVet sensors (m2m Imaging; Newark, NJ, USA) to allow for adjustments of isoflurane dose. A multimodal SPECT/CT scanner (VECTor; MILabs, Houten, Netherlands) fitted with an extra-ultrahigh sensitivity mouse pinhole collimator was

used for the study. Following each SPECT acquisition, a whole-body CT scan (55 kV, 615 μA) was recorded for anatomical information. *Image Reconstruction*: SPECT data were reconstructed using a pixel-based ordered subset expectation maximization (POSEM) algorithm with 6 iterations and 16 subsets with a voxel size defined as 0.4 mm^3 using U-SPECT Rec2.5li software (MILabs).[91] The ^{111}In photopeak window was centered at 171 keV with a 20% energy window width (background weight, 2.5). The SPECT images were decay corrected to the start of each acquisition, and after CT registration, attenuation correction was applied. For visual representation, the reconstructed volumes of SPECT scans were postfiltered with a 3D Gaussian filter using AMIDE (UCLA; Los Angeles, CA, USA),[92] (Kernel size, 15; fwhm, 1). A cone-beam filtered back-projection algorithm was used to reconstruct the CT data into a 3D image on a 0.169 mm^3 voxel grid with SkyScan NRecon software (Micro Photonics Inc.; Allentown, PA, USA). *Image Analysis*: The SPECT data set was quantified using AMIDE. Volumes of interest (VOIs) were drawn in the left ventricle of the heart (blood pool) and liver ($n = 3$), VOIs were also placed over the urinary bladder and the tumor region. A calibration factor, obtained by scanning a point source phantom containing a known concentration of ^{111}In, was used to convert the VOI data from scanner units (counts/voxel) to units of radioactivity concentration (MBq/mL). VOI data were decay corrected to the time of injection. SUV$_{mean}$, SUV$_{max}$, and SUV$_{95th}$ (average intensity, highest intensity voxel, and median of upper 10% of highest intensity pixels in VOI,[82] respectively) were calculated according to eq 1.

$$SUV_{mean,max,95th} \left(\frac{g}{mL} \right)$$
$$= \frac{\text{mean,max,95th activity conc. in VOI} \left(\frac{MBq}{mL} \right) \times \text{animal weight (g)}}{\text{injected radioactive dose (MBq)}}$$

(1)

Total activity in VOI was calculated according to eq 2.

$$\%ID = \frac{\text{mean activity conc. in VOI} \left(\frac{MBq}{mL} \right) \times \text{VOI volume (mL)}}{\text{injected radioactive dose (MBq)}} \times 100$$

(2)

Ex Vivo Biodistribution. Immediately after the last SPECT/CT scan, animals were sacrificed via CO$_2$ asphyxiation under isoflurane anesthesia. Cardiac puncture was performed to recover blood, and the following organs of interest were dissected out: heart, lungs, liver, kidney, urinary bladder, stomach, small intestine, large intestine, brain, spleen, pancreas, muscle, bone (femur and joint), and tumor, which were cleaned and weighed. The activity was quantified using a calibrated Cobra II Autogamma counter (Packard Instruments). For those organs that could not be completely dissected out—muscle, bone, and blood—total organ weights were obtained by multiplying the %ID/g value by standardized organ weights or volumes for age- and sex-matched mice.[93,94] *Pharmacokinetic Modeling*: The PKSolver[95] add-in for Microsoft Excel with IV bolus modeling was used to calculate blood and liver half-life for the three tested formulations.

Histology. Following weighing and γ counting, sections of heart, lung, liver, spleen, and tumor were fixed in 10% neutral buffered formalin solution over a 3 day period and stored for 10 half-lives to allow for decay of ^{111}In. Organs were embedded in paraffin, sliced into 4 μM thick sections, stained with

hematoxylin and eosin (H&E), and scanned at 20× magnification on a VS 120 slide scanner (Evident; Tokyo, Japan) according to standard laboratory practice at the histology core at the UBC Centre for Comparative Medicine (CCM). Slices used for confocal imaging were mounted directly with ProLong Diamond Antifade Mountant with DAPI to counterstain nuclei and imaged on a Zeiss LSM 700 laser scanning confocal microscope (ZEISS AG).

Statistical Analysis. Results are presented as mean ± SD; $n = 3$. Statistical analysis for in vivo experiments was performed using two-way ANOVA with repeated measurements and a Holm-Sidak correction. Statistics for pretargeted click reaction of $[^{111}In]In$-Tz-DTPA with HPG-sgc8 and HPG-scr were calculated using paired sample t test. Probability values of $p < 0.05$ were considered statistically significant.

■ ASSOCIATED CONTENT

ⓢ Supporting Information

The Supporting Information is available free of charge at https://pubs.acs.org/doi/10.1021/acsomega.2c07762.

TCO moieties determinations (Figure S1); flow cytometry gating strategy (Figure S2); competition binding (Figure S3); HPG-Cy5 temperature dependence (Figure S4); temperature effects on bindings (Figure S5); pretargeted in vitro labeling images (Figure S6); cell morphologies (Figure S7); representative SPECT/CT MIP renderings of injected mice (Figure S8); activity profile of injected mouse (Figure S9); plasma stability (Figure S10); organs histologies (Figure S11); ^1H NMR spectrum (Figure S12) (PDF)

■ AUTHOR INFORMATION

Corresponding Authors

Katayoun Saatchi − *Faculty of Pharmaceutical Sciences, University of British Columbia, Vancouver, British Columbia V6T 1Z3, Canada;* ◉ orcid.org/0000-0002-5372-6791; Email: kathy.saatchi@ubc.ca

Urs O. Häfeli − *Faculty of Pharmaceutical Sciences, University of British Columbia, Vancouver, British Columbia V6T 1Z3, Canada; Department of Pharmacy, Faculty of Health and Medical Sciences, University of Copenhagen, 2100 Copenhagen, Denmark;* ◉ orcid.org/0000-0003-0671-4509; Email: urs.hafeli@ubc.ca

Authors

Lennart Bohrmann − *Faculty of Pharmaceutical Sciences, University of British Columbia, Vancouver, British Columbia V6T 1Z3, Canada; Department of Pharmacy, Faculty of Health and Medical Sciences, University of Copenhagen, 2100 Copenhagen, Denmark*

Tobias Burghardt − *Faculty of Pharmaceutical Sciences, University of British Columbia, Vancouver, British Columbia V6T 1Z3, Canada*

Cristina Rodríguez-Rodríguez − *Faculty of Pharmaceutical Sciences, University of British Columbia, Vancouver, British Columbia V6T 1Z3, Canada;* ◉ orcid.org/0000-0002-3313-4422

Matthias M. Herth − *Department of Drug Design and Pharmacology, Faculty of Health and Medicinal Sciences, University of Copenhagen, 2100 Copenhagen, Denmark; Department of Clinical Physiology, Nuclear Medicine & PET,*

Rigshospitalet, 2100 Copenhagen, Denmark; ◉ orcid.org/0000-0002-7788-513X

Complete contact information is available at:
https://pubs.acs.org/10.1021/acsomega.2c07762

Author Contributions

L.B. and U.O.H. designed the experiments. L.B. analyzed the data. L.B., T.B., C.R.-R., and K.S. performed the experiments. K.S. synthesized and characterized HPG-NH$_2$. M.M.H. oversaw synthesis of Tz-NHS. L.B. and T.B. performed flow cytometry. L.B. characterized HPG-aptamer formulations and performed confocal microscopy and cytotoxicity studies. K.S. and L.B. performed radiolabeling. C.R.-R. performed SPECT/CT reconstructions. L.B. and C.R.-R. performed SPECT/CT, biodistribution, and histology studies and analyzed the data. L.B. and U.O.H. drafted the manuscript. All authors revised and approved the final manuscript. M.M.H. and U.O.H. oversaw the research.

Notes

The authors declare no competing financial interest.

■ ACKNOWLEDGMENTS

■ ABBREVIATIONS

CCK4, colon carcinoma kinase 4; CT, computed tomography; DAPI, 4′,6-diamidino-2-phenylindole; DTPA, diethylenetriaminepentaacetic acid; EDC, 1-Ethyl-3-(3-(dimethylamino)-propyl)carbodiimide; EPR, enhanced permeation and retention; H&E, hematoxylin and eosin; HPG, hyperbranched polyglycerol; HPLC, high-performance liquid chromatography; IEDDA, inverse electron demand Diels−Alder; ITLC, instant-thin-layer chromatography; kDa, kilodalton; keV, kiloelectron-volt; MBq, megabecquerel; MIP, maximum intensity projection; MW, molecular weight; MWCO, molecular weight cutoff; NHS, N-hydroxysuccinimide; NP, nanoparticle; PET, positron emission tomography; PTK7, protein tyrosine kinase 7; SPECT, single-photon emission computed tomography; ssDNA, single-stranded DNA; SUV, standardized uptake

value; TCO, *trans*-cyclooctene; Tz, tetrazine; VOI, volume of interest

■ REFERENCES

(1) Lee, D.-E.; Koo, H.; Sun, I.-C.; Ryu, J. H.; Kim, K.; Kwon, I. C. Multifunctional nanoparticles for multimodal imaging and theragnosis. *Chem. Soc. Rev.* **2012**, *41* (7), 2656−2672.

(2) Key, J.; Leary, J. F. Nanoparticles for multimodal in vivo imaging in nanomedicine. *Int. J. Nanomed.* **2014**, *9*, 711−726.

(3) Chapman, S.; Dobrovolskaia, M.; Farahani, K.; Goodwin, A.; Joshi, A.; Lee, H.; Meade, T.; Pomper, M.; Ptak, K.; Rao, J.; Singh, R.; Sridhar, S.; Stern, S.; Wang, A.; Weaver, J. B.; Woloschak, G.; Yang, L. Nanoparticles for cancer imaging: The good, the bad, and the promise. *Nano Today* **2013**, *8* (5), 454−460.

(4) Reisch, A.; Klymchenko, A. S. Fluorescent Polymer Nanoparticles Based on Dyes: Seeking Brighter Tools for Bioimaging. *Small* **2016**, *12* (15), 1968−1992.

(5) Kainthan, R. K.; Muliawan, E. B.; Hatzikiriakos, S. G.; Brooks, D. E. Synthesis, Characterization, and Viscoelastic Properties of High Molecular Weight Hyperbranched Polyglycerols. *Macromolecules* **2006**, *39* (22), 7708−7717.

(6) Abbina, S.; Vappala, S.; Kumar, P.; Siren, E. M. J.; La, C. C.; Abbasi, U.; Brooks, D. E.; Kizhakkedathu, J. N. Hyperbranched polyglycerols: recent advances in synthesis, biocompatibility and biomedical applications. *J. Mater. Chem. B* **2017**, *5* (47), 9249−9277.

(7) Schmitt, V.; Rodríguez-Rodríguez, C.; Hamilton, J. L.; Shenoi, R. A.; Schaffer, P.; Sossi, V.; Kizhakkedathu, J. N.; Saatchi, K.; Häfeli, U. O. Quantitative SPECT imaging and biodistribution point to molecular weight independent tumor uptake for some long-circulating polymer nanocarriers. *RSC Adv.* **2018**, *8* (10), 5586−5595.

(8) Saatchi, K.; Gelder, N.; Gershkovich, P.; Sivak, O.; Wasan, K. M.; Kainthan, R. K.; Brooks, D. E.; Häfeli, U. O. Long-circulating non-toxic blood pool imaging agent based on hyperbranched polyglycerols. *Int. J. Pharm.* **2012**, *422* (1−2), 418−427.

(9) Saatchi, K.; Soema, P.; Gelder, N.; Misri, R.; McPhee, K.; Baker, J. H. E.; Reinsberg, S. A.; Brooks, D. E.; Häfeli, U. O. Hyperbranched Polyglycerols as Trimodal Imaging Agents: Design, Biocompatibility, and Tumor Uptake. *Bioconjugate Chem.* **2012**, *23* (3), 372−381.

(10) Baker, J. H. E.; McPhee, K. C.; Moosvi, F.; Saatchi, K.; Häfeli, U. O.; Minchinton, A. I.; Reinsberg, S. A. Multi-modal magnetic resonance imaging and histology of vascular function in xenografts using macromolecular contrast agent hyperbranched polyglycerol (HPG-GdF). *Contrast Media Mol. Imaging* **2016**, *11* (1), 77−88.

(11) Bohrmann, L.; Burghardt, T.; Haynes, C.; Saatchi, K.; Häfeli, U. O. Aptamers used for molecular imaging and theranostics - recent developments. *Theranostics* **2022**, *12* (9), 4010−4050.

(12) Bouvier-Müller, A.; Ducongé, F. Application of aptamers for in vivo molecular imaging and theranostics. *Adv. Drug Delivery Rev.* **2018**, *134*, 94−106.

(13) Shangguan, D.; Li, Y.; Tang, Z.; Cao, Z. C.; Chen, H. W.; Mallikaratchy, P.; Sefah, K.; Yang, C. J.; Tan, W. Aptamers evolved from live cells as effective molecular probes for cancer study. *Proc. Natl. Acad. Sci. U. S. A.* **2006**, *103* (32), 11838−11843.

(14) Shangguan, D.; Cao, Z.; Meng, L.; Mallikaratchy, P.; Sefah, K.; Wang, H.; Li, Y.; Tan, W. Cell-specific aptamer probes for membrane protein elucidation in cancer cells. *J. Proteome Res.* **2008**, *7* (5), 2133−2139.

(15) Mossie, K.; Jallal, B.; Alves, F.; Sures, I.; Plowman, G. D.; Ullrich, A. Colon carcinoma kinase-4 defines a new subclass of the receptor tyrosine kinase family. *Oncogene* **1995**, *11* (10), 2179−2184.

(16) Lhoumeau, A. C.; Martinez, S.; Boher, J. M.; Monges, G.; Castellano, R.; Goubard, A.; Doremus, M.; Poizat, F.; Lelong, B.; de Chaisemartin, C.; Bardin, F.; Viens, P.; Raoul, J. L.; Prebet, T.; Aurrand-Lions, M.; Borg, J. P.; Gonçalves, A. Overexpression of the Promigratory and Prometastatic PTK7 Receptor Is Associated with an Adverse Clinical Outcome in Colorectal Cancer. *PLoS One* **2015**, *10* (5), e0123768.

(17) Easty, D. J.; Mitchell, P. J.; Patel, K.; Florenes, V. A.; Spritz, R. A.; Bennett, D. C. Loss of expression of receptor tyrosine kinase family genes PTK7 and SEK in metastatic melanoma. *Int. J. Cancer* **1997**, *71* (6), 1061−1065.

(18) Müller-Tidow, C.; Schwäble, J.; Steffen, B. r.; Tidow, N.; Brandt, B.; Becker, K.; Schulze-Bahr, E.; Halfter, H.; Vogt, U.; Metzger, R.; Schneider, P. M.; Büchner, T.; Brandts, C.; Berdel, W. E.; Serve, H. High-Throughput Analysis of Genome-Wide Receptor Tyrosine Kinase Expression in Human Cancers Identifies Potential Novel Drug Targets. *Clin. Cancer Res.* **2004**, *10* (4), 1241−1249.

(19) Prebet, T.; Lhoumeau, A. C.; Arnoulet, C.; Aulas, A.; Marchetto, S.; Audebert, S.; Puppo, F.; Chabannon, C.; Sainty, D.; Santoni, M. J.; Sebbagh, M.; Summerour, V.; Huon, Y.; Shin, W. S.; Lee, S. T.; Esterni, B.; Vey, N.; Borg, J. P. The cell polarity PTK7 receptor acts as a modulator of the chemotherapeutic response in acute myeloid leukemia and impairs clinical outcome. *Blood* **2010**, *116* (13), 2315−2323.

(20) Gobble, R. M.; Qin, L. X.; Brill, E. R.; Angeles, C. V.; Ugras, S.; O'Connor, R. B.; Moraco, N. H.; Decarolis, P. L.; Antonescu, C.; Singer, S. Expression profiling of liposarcoma yields a multigene predictor of patient outcome and identifies genes that contribute to liposarcomagenesis. *Cancer Res.* **2011**, *71* (7), 2697−2705.

(21) Lin, Y.; Zhang, L.-H.; Wang, X.-H.; Xing, X.-F.; Cheng, X.-J.; Dong, B.; Hu, Y.; Du, H.; Li, Y.-A.; Zhu, Y.-B.; Ding, N.; Du, Y.-X.; Li, J.-Y.; Ji, J.-F. PTK7 as a novel marker for favorable gastric cancer patient survival. *J. Surg. Oncol.* **2012**, *106* (7), 880−886.

(22) Ataseven, B.; Gunesch, A.; Eiermann, W.; Kates, R. E.; Högel, B.; Knyazev, P.; Ullrich, A.; Harbeck, N. PTK7 as a potential prognostic and predictive marker of response to adjuvant chemotherapy in breast cancer patients, and resistance to anthracycline drugs. *OncoTargets Ther.* **2014**, *7*, 1723−1731.

(23) Shi, H.; He, X.; Wang, K.; Wu, X.; Ye, X.; Guo, Q.; Tan, W.; Qing, Z.; Yang, X.; Zhou, B. Activatable aptamer probe for contrast-enhanced in vivo cancer imaging based on cell membrane protein-triggered conformation alteration. *Proc. Natl. Acad. Sci. U. S. A.* **2011**, *108* (10), 3900−3905.

(24) Lei, Y.; Qiao, Z.; Tang, J.; He, X.; Shi, H.; Ye, X.; Yan, L. a.; He, D.; Wang, K. DNA nanotriangle-scaffolded activatable aptamer probe with ultralow background and robust stability for cancer theranostics. *Theranostics* **2018**, *8* (15), 4062−4071.

(25) Zhu, G.; Zheng, J.; Song, E.; Donovan, M.; Zhang, K.; Liu, C.; Tan, W. Self-assembled, aptamer-tethered DNA nanotrains for targeted transport of molecular drugs in cancer theranostics. *Proc. Natl. Acad. Sci. U. S. A.* **2013**, *110* (20), 7998−8003.

(26) Lei, Y.; Tang, J.; Shi, H.; Ye, X.; He, X.; Xu, F.; Yan, L. a.; Qiao, Z.; Wang, K. Nature-Inspired Smart DNA Nanodoctor for Activatable In Vivo Cancer Imaging and In Situ Drug Release Based on Recognition-Triggered Assembly of Split Aptamer. *Anal. Chem.* **2016**, *88* (23), 11699−11706.

(27) Ye, X.; Shi, H.; He, X.; Yu, Y.; He, D.; Tang, J.; Lei, Y.; Wang, K. Cu−Au alloy nanostructures coated with aptamers: a simple, stable and highly effective platform for in vivo cancer theranostics. *Nanoscale* **2016**, *8* (4), 2260−2267.

(28) Lei, Y.; He, X.; Tang, J.; Shi, H.; He, D.; Yan, L. a.; Liu, J.; Zeng, Y.; Wang, K. Ultra-pH-responsive split i-motif based aptamer anchoring strategy for specific activatable imaging of acidic tumor microenvironment. *Chem. Commun.* **2018**, *54* (73), 10288−10291.

(29) Fang, Z.; Wang, X.; Sun, Y.; Fan, R.; Liu, Z.; Guo, R.; Xie, D. Sgc8 aptamer targeted glutathione-responsive nanoassemblies containing Ara-C prodrug for the treatment of acute lymphoblastic leukemia. *Nanoscale* **2019**, *11* (47), 23000−23012.

(30) Sicco, E.; Baez, J.; Ibarra, M.; Fernández, M.; Cabral, P.; Moreno, M.; Cerecetto, H.; Calzada, V. Sgc8-c Aptamer as a Potential Theranostic Agent for Hemato-Oncological Malignancies. *Cancer Biother.Radiopharm.* **2020**, *35* (4), 262−270.

(31) Castelli, R.; Ibarra, M.; Faccio, R.; Miraballes, I.; Fernández, M.; Moglioni, A.; Cabral, P.; Cerecetto, H.; Glisoni, R. J.; Calzada, V. T908 Polymeric Micelles Improved the Uptake of Sgc8-c Aptamer Probe in Tumor-Bearing Mice: A Co-Association Study between the Probe and Preformed Nanostructures. *Pharmaceuticals (Basel)* **2022**, *15* (1), 15.

(32) Liu, C.; Zheng, J.; Deng, L.; Ma, C.; Li, J.; Li, Y.; Yang, S.; Yang, J.; Wang, J.; Yang, R. Targeted Intracellular Controlled Drug Delivery and Tumor Therapy through in Situ Forming Ag Nanogates on Mesoporous Silica Nanocontainers. *ACS Appl. Mater. Interfaces* **2015**, *7* (22), 11930−11938.

(33) Yan, L. a.; Shi, H.; He, X.; Wang, K.; Tang, J.; Chen, M.; Ye, X.; Xu, F.; Lei, Y. A Versatile Activatable Fluorescence Probing Platform for Cancer Cells in Vitro and in Vivo Based on Self-Assembled Aptamer/Carbon Nanotube Ensembles. *Anal. Chem.* **2014**, *86* (18), 9271−9277.

(34) Xia, F.; He, A.; Zhao, H.; Sun, Y.; Duan, Q.; Abbas, S. J.; Liu, J.; Xiao, Z.; Tan, W. Molecular Engineering of Aptamer Self-Assemblies Increases in Vivo Stability and Targeted Recognition. *ACS Nano* **2022**, *16* (1), 169−179.

(35) Wang, L.; Jacobson, O.; Avdic, D.; Rotstein, B. H.; Weiss, I. D.; Collier, L.; Chen, X.; Vasdev, N.; Liang, S. H. Ortho-Stabilized 18F-Azido Click Agents and their Application in PET Imaging with Single-Stranded DNA Aptamers. *Angew. Chem., Int. Ed.* **2015**, *54* (43), 12777−12781.

(36) Ding, D.; Yang, C.; Lv, C.; Li, J.; Tan, W. Improving Tumor Accumulation of Aptamers by Prolonged Blood Circulation. *Anal. Chem.* **2020**, *92* (5), 4108−4114.

(37) Jacobson, O.; Weiss, I. D.; Wang, L.; Wang, Z.; Yang, X.; Dewhurst, A.; Ma, Y.; Zhu, G.; Niu, G.; Kiesewetter, D. O.; Vasdev, N.; Liang, S. H.; Chen, X. 18F-Labeled Single-Stranded DNA Aptamer for PET Imaging of Protein Tyrosine Kinase-7 Expression. *J. Nucl. Med.* **2015**, *56* (11), 1780−1785.

(38) Arévalo, A. P.; Castelli, R.; Ibarra, M.; Crispo, M.; Calzada, V. In Vivo Evaluation of Sgc8-c Aptamer as a Molecular Imaging Probe for Colon Cancer in a Mouse Xenograft Model. *Int. J. Mol. Sci.* **2022**, *23* (5), 2466.

(39) Wang, D.; Peng, Y.; Deng, Z.; Tan, Y.; Su, Y.; Kuai, H.; Ai, L.; Huang, Z.; Wang, X.-Q.; Zhang, X.; Tan, W. Modularly Engineered Solid-Phase Synthesis of Aptamer-Functionalized Small Molecule Drugs for Targeted Cancer Therapy. *Adv. Ther.* **2020**, *3* (9), 2000074.

(40) Meng, H.-M.; Hu, X.-X.; Kong, G.-Z.; Yang, C.; Fu, T.; Li, Z.-H.; Zhang, X.-B. Aptamer-functionalized nanoscale metal-organic frameworks for targeted photodynamic therapy. *Theranostics* **2018**, *8* (16), 4332−4344.

(41) Zhang, L.; Abdullah, R.; Hu, X.; Bai, H.; Fan, H.; He, L.; Liang, H.; Zou, J.; Liu, Y.; Sun, Y.; Zhang, X.; Tan, W. Engineering of Bioinspired, Size-Controllable, Self-Degradable Cancer-Targeting DNA Nanoflowers via the Incorporation of an Artificial Sandwich Base. *J. Am. Chem. Soc.* **2019**, *141* (10), 4282−4290.

(42) Zhang, Y.; Chen, W.; Fang, Y.; Zhang, X.; Liu, Y.; Ju, H. Activating a DNA Nanomachine via Computation across Cancer Cell Membranes for Precise Therapy of Solid Tumors. *J. Am. Chem. Soc.* **2021**, *143* (37), 15233−15242.

(43) Sicco, E.; Mónaco, A.; Fernandez, M.; Moreno, M.; Calzada, V.; Cerecetto, H. Metastatic and non-metastatic melanoma imaging using Sgc8-c aptamer PTK7-recognizer. *Sci. Rep.* **2021**, *11* (1), 19942.

(44) Blankenberg, F. G.; Strauss, H. W. Nuclear medicine applications in molecular imaging. *J. Magn. Reson. Imaging* **2002**, *16* (4), 352−361.

(45) Conway, J. R. W.; Carragher, N. O.; Timpson, P. Developments in preclinical cancer imaging: innovating the discovery of therapeutics. *Nat. Rev. Cancer* **2014**, *14* (5), 314−328.

(46) Culver, J.; Akers, W.; Achilefu, S. Multimodality Molecular Imaging with Combined Optical and SPECT/PET Modalities. *J. Nucl. Med.* **2008**, *49* (2), 169−172.

(47) Kolb, H. C.; Finn, M. G.; Sharpless, K. B. Click Chemistry: Diverse Chemical Function from a Few Good Reactions. *Angew. Chem., Int. Ed.* **2001**, *40* (11), 2004−2021.

(48) Nwe, K.; Brechbiel, M. W. Growing applications of "click chemistry" for bioconjugation in contemporary biomedical research. *Cancer Biother.Radiopharm.* **2009**, *24* (3), 289−302.

(49) McKay, C. S.; Finn, M. G. Click Chemistry in Complex Mixtures: Bioorthogonal Bioconjugation. *Chem. Biol.* **2014**, *21* (9), 1075−1101.

(50) Meyer, J.-P.; Adumeau, P.; Lewis, J. S.; Zeglis, B. M. Click Chemistry and Radiochemistry: The First 10 Years. *Bioconjugate Chem.* **2016**, *27* (12), 2791−2807.

(51) Zhou, J.; Rossi, J. Aptamers as targeted therapeutics: current potential and challenges. *Nat. Rev. Drug Discov* **2017**, *16* (3), 181−202.

(52) Shahidi-Hamedani, N.; Shier, W. T.; Moghadam Ariaee, F.; Abnous, K.; Ramezani, M. Targeted gene delivery with noncovalent electrostatic conjugates of sgc-8c aptamer and polyethylenimine. *J. Gene Med.* **2013**, *15* (6−7), 261−269.

(53) Liu, Y.; Bae, S. W.; Wang, K.; Hong, J.-I.; Zhu, Z.; Tan, W.; Pappas, D. The effects of flow type on aptamer capture in differential mobility cytometry cell separations. *Anal. Chim. Acta* **2010**, *673* (1), 95−100.

(54) Chen, Y.; Munteanu, A. C.; Huang, Y.-F.; Phillips, J.; Zhu, Z.; Mavros, M.; Tan, W. Mapping receptor density on live cells by using fluorescence correlation spectroscopy. *Chemistry* **2009**, *15* (21), 5327−5336.

(55) Zhao, Y.; Hu, S.; Wang, H.; Yu, K.; Guan, Y.; Liu, X.; Li, N.; Liu, F. DNA Dendrimer−Streptavidin Nanocomplex: an Efficient Signal Amplifier for Construction of Biosensing Platforms. *Anal. Chem.* **2017**, *89* (12), 6907−6914.

(56) Lin, S.; Gao, W.; Tian, Z.; Yang, C.; Lu, L.; Mergny, J.-L.; Leung, C.-H.; Ma, D.-L. Luminescence switch-on detection of protein tyrosine kinase-7 using a G-quadruplex-selective probe. *Chem. Sci.* **2015**, *6* (7), 4284−4290.

(57) Li, S.; Wang, K.; Hao, S.; Dang, F.; Zhang, Z.-Q.; Zhang, J. Antifouling Gold-Inlaid BSA Coating for the Highly Efficient Capture of Circulating Tumor Cells. *Anal. Chem.* **2022**, *94*, 6754−6759.

(58) Li, Z.; Zhou, Z.; Xue, N.; Wu, S.; Miao, X. Electrochemical aptamer-based determination of protein tyrosine kinase-7 using toehold-mediated strand displacement amplification on gold nano-particles and graphene oxide. *Microchim. Acta* **2019**, *186* (11), 720.

(59) Yazdian-Robati, R.; Arab, A.; Ramezani, M.; Abnous, K.; Taghdisi, S. M. Application of aptamers in treatment and diagnosis of leukemia. *Int. J. Pharm.* **2017**, *529* (1), 44−54.

(60) Kelly, L.; Maier, K. E.; Yan, A.; Levy, M. A comparative analysis of cell surface targeting aptamers. *Nat. Commun.* **2021**, *12* (1), 6275.

(61) Siddiqui, S.; Yuan, J. Binding Characteristics Study of DNA based Aptamers for E. coli O157:H7. *Molecules* **2021**, *26* (1), 204.

(62) Bottari, F.; Daems, E.; de Vries, A.-M.; Van Wielendaele, P.; Trashin, S.; Blust, R.; Sobott, F.; Madder, A.; Martins, J. C.; De Wael, K. Do Aptamers Always Bind? The Need for a Multifaceted Analytical Approach When Demonstrating Binding Affinity between Aptamer and Low Molecular Weight Compounds. *J. Am. Chem. Soc.* **2020**, *142* (46), 19622−19630.

(63) Padlan, C. S.; Malashkevich, V. N.; Almo, S. C.; Levy, M.; Brenowitz, M.; Girvin, M. E. An RNA aptamer possessing a novel monovalent cation-mediated fold inhibits lysozyme catalysis by inhibiting the binding of long natural substrates. *Rna* **2014**, *20* (4), 447−461.

(64) Zhao, Q.; Matson, S.; Herrera, C. J.; Fisher, E.; Yu, H.; Krieg, A. M. Comparison of Cellular Binding and Uptake of Antisense Phosphodiester, Phosphorothioate, and Mixed Phosphorothioate and Methylphosphonate Oligonucleotides. *Antisense Res. Dev.* **1993**, *3* (1), 53−66.

(65) Raddatz, M.-S. L.; Dolf, A.; Endl, E.; Knolle, P.; Famulok, M.; Mayer, G. Enrichment of Cell-Targeting and Population-Specific Aptamers by Fluorescence-Activated Cell Sorting. *Angew. Chem., Int. Ed.* **2008**, *47* (28), 5190−5193.

(66) Avci-Adali, M.; Metzger, M.; Perle, N.; Ziemer, G.; Wendel, H. P. Ptifalls of Cell-Sytematic Evolution of Ligands by Exponential Enrichment (SELEX): Existing Dead Cells During In Vitro Selection Anticipate the Enrichment of Specific Aptamers. *Oligonucleotides* **2010**, *20* (6), 317−323.

(67) Flanagan, S. P.; Fogel, R.; Edkins, A. L.; Ho, L. S. J.; Limson, J. Nonspecific nuclear uptake of anti-MUC1 aptamers by dead cells: the role of cell viability monitoring in aptamer targeting of membrane-

bound protein cancer biomarkers. *Anal. Methods* **2021**, *13* (9), 1191−1203.

(68) Carothers, J. M.; Oestreich, S. C.; Szostak, J. W. Aptamers selected for higher-affinity binding are not more specific for the target ligand. *J. Am. Chem. Soc.* **2006**, *128* (24), 7929−7937.

(69) McKeague, M.; De Girolamo, A.; Valenzano, S.; Pascale, M.; Ruscito, A.; Velu, R.; Frost, N. R.; Hill, K.; Smith, M.; McConnell, E. M.; DeRosa, M. C. Comprehensive Analytical Comparison of Strategies Used for Small Molecule Aptamer Evaluation. *Anal. Chem.* **2015**, *87* (17), 8608−8612.

(70) Ray, P.; White, R. R. Cell-SELEX Identifies a "Sticky" RNA Aptamer Sequence. *J. Nucleic Acids* **2017**, *2017*, 4943072.

(71) Reyes-Reyes, E. M.; Teng, Y.; Bates, P. J. A new paradigm for aptamer therapeutic AS1411 action: uptake by macropinocytosis and its stimulation by a nucleolin-dependent mechanism. *Cancer Res.* **2010**, *70* (21), 8617−8629.

(72) Sefah, K.; Shangguan, D.; Xiong, X.; O'Donoghue, M. B.; Tan, W. Development of DNA aptamers using Cell-SELEX. *Nat. Protoc.* **2010**, *5* (6), 1169−1185.

(73) Sefah, K.; Tang, Z. W.; Shangguan, D. H.; Chen, H.; Lopez-Colon, D.; Li, Y.; Parekh, P.; Martin, J.; Meng, L.; Phillips, J. A.; Kim, Y. M.; Tan, W. H. Molecular recognition of acute myeloid leukemia using aptamers. *Leukemia* **2009**, *23* (2), 235−244.

(74) Bouchard, P. R.; Hutabarat, R. M.; Thompson, K. M. Discovery and Development of Therapeutic Aptamers. *Annu. Rev. Pharmacol. Toxicol.* **2010**, *50* (1), 237−257.

(75) Kainthan, R. K.; Brooks, D. E. In vivo biological evaluation of high molecular weight hyperbranched polyglycerols. *Biomaterials* **2007**, *28* (32), 4779−4787.

(76) Du, C.; Mendelson, A. A.; Guan, Q.; Dairi, G.; Chafeeva, I.; da Roza, G.; Kizhakkedathu, J. N. Hyperbranched polyglycerol is superior to glucose for long-term preservation of peritoneal membrane in a rat model of chronic peritoneal dialysis. *J. Transl. Med.* **2016**, *14* (1), 338.

(77) Chapanian, R.; Constantinescu, I.; Medvedev, N.; Scott, M. D.; Brooks, D. E.; Kizhakkedathu, J. N. Therapeutic Cells via Functional Modification: Influence of Molecular Properties of Polymer Grafts on In Vivo Circulation, Clearance, Immunogenicity, and Antigen Protection. *Biomacromolecules* **2013**, *14* (6), 2052−2062.

(78) Kainthan, R. K.; Gnanamani, M.; Ganguli, M.; Ghosh, T.; Brooks, D. E.; Maiti, S.; Kizhakkedathu, J. N. Blood compatibility of novel water soluble hyperbranched polyglycerol-based multivalent cationic polymers and their interaction with DNA. *Biomaterials* **2006**, *27* (31), 5377−5390.

(79) Griffin, L. C.; Tidmarsh, G. F.; Bock, L. C.; Toole, J. J.; Leung, L. L. In vivo anticoagulant properties of a novel nucleotide-based thrombin inhibitor and demonstration of regional anticoagulation in extracorporeal circuits. *Blood* **1993**, *81* (12), 3271−3276.

(80) Hicke, B. J.; Stephens, A. W.; Gould, T.; Chang, Y.-F.; Lynott, C. K.; Heil, J.; Borkowski, S.; Hilger, C.-S.; Cook, G.; Warren, S.; Schmidt, P. G. Tumor Targeting by an Aptamer. *J. Nucl. Med.* **2006**, *47* (4), 668−678.

(81) Adhipandito, C. F.; Cheung, S. H.; Lin, Y. H.; Wu, S. H. Atypical Renal Clearance of Nanoparticles Larger Than the Kidney Filtration Threshold. *Int. J. Mol. Sci.* **2021**, *22* (20), 11182.

(82) Baiocco, S.; Matteucci, F.; Mezzenga, E.; Caroli, P.; Di Iorio, V.; Cittanti, C.; Bevilacqua, A.; Paganelli, G.; Sarnelli, A. SUV(95th) as a Reliable Alternative to SUV(max) for Determining Renal Uptake in [(68)Ga] PSMA PET/CT. *Mol. Imaging Biol.* **2020**, *22* (4), 1070−1077.

(83) Calzada, V.; Moreno, M.; Newton, J.; González, J.; Fernández, M.; Gambini, J. P.; Ibarra, M.; Chabalgoity, A.; Deutscher, S.; Quinn, T.; Cabral, P.; Cerecetto, H. Development of new PTK7-targeting aptamer-fluorescent and -radiolabelled probes for evaluation as molecular imaging agents: Lymphoma and melanoma in vivo proof of concept. *Bioorg. Med. Chem.* **2017**, *25* (3), 1163−1171.

(84) McGinely, N. L.; Plumb, J. A.; Wheate, N. J. DNA-based aptamer fails as a simultaneous cancer targeting agent and drug

delivery vehicle for a phenanthroline-based platinum(II) complex. *J. Inorg. Biochem.* **2013**, *128*, 124−130.

(85) Sauter, A. W.; Mansi, R.; Hassiepen, U.; Muller, L.; Panigada, T.; Wiehr, S.; Wild, A.-M.; Geistlich, S.; Béhé, M.; Rottenburger, C.; Wild, D.; Fani, M. Targeting of the Cholecystokinin-2 Receptor with the Minigastrin Analog ^{177}Lu-DOTA-PP-F11N: Does the Use of Protease Inhibitors Further Improve In Vivo Distribution? *J. Nucl. Med.* **2019**, *60* (3), 393−399.

(86) Kunjachan, S.; Pola, R.; Gremse, F.; Theek, B.; Ehling, J.; Moeckel, D.; Hermanns-Sachweh, B.; Pechar, M.; Ulbrich, K.; Hennink, W. E.; Storm, G.; Lederle, W.; Kiessling, F.; Lammers, T. Passive versus Active Tumor Targeting Using RGD- and NGR-Modified Polymeric Nanomedicines. *Nano Lett.* **2014**, *14* (2), 972−981.

(87) Fletcher, N. L.; Houston, Z. H.; Simpson, J. D.; Veedu, R. N.; Thurecht, K. J. Designed multifunctional polymeric nanomedicines: long-term biodistribution and tumour accumulation of aptamer-targeted nanomaterials. *Chem. Commun.* **2018**, *54* (82), 11538−11541.

(88) Yang, J.; Karver, M. R.; Li, W.; Sahu, S.; Devaraj, N. K. Metal-Catalyzed One-Pot Synthesis of Tetrazines Directly from Aliphatic Nitriles and Hydrazine. *Angew. Chem., Int. Ed.* **2012**, *51* (21), 5222−5225.

(89) Maggi, A.; Ruivo, E.; Fissers, J.; Vangestel, C.; Chatterjee, S.; Joossens, J.; Sobott, F.; Staelens, S.; Stroobants, S.; Van Der Veken, P.; wyffels, L.; Augustyns, K. Development of a novel antibody−tetrazine conjugate for bioorthogonal pretargeting. *Org. Biomol. Chem.* **2016**, *14* (31), 7544−7551.

(90) Summer, H.; Grämer, R.; Dröge, P., Denaturing urea polyacrylamide gel electrophoresis (Urea PAGE). *J. Vis. Exp.* **2009**, *32*. DOI: 10.3791/1485-v.

(91) Branderhorst, W.; Vastenhouw, B.; Beekman, F. J. Pixel-based subsets for rapid multi-pinhole SPECT reconstruction. *Phys. Med. Biol.* **2010**, *55* (7), 2023−2034.

(92) Loening, A. M.; Gambhir, S. S. AMIDE: a free software tool for multimodality medical image analysis. *Mol. Imaging* **2003**, *2* (3), 131−137.

(93) Davies, B.; Morris, T. Physiological Parameters in Laboratory Animals and Humans. *Pharm. Res.* **1993**, *10* (7), 1093−1095.

(94) Hoyt, R. E.; Hawkins, J. V.; St Clair, M. B.; Kennet, M. J., Mouse Physiology. In *The Mouse in Biomedical Research*, 2nd ed.; Fox, J. G., Davisson, M. T., Quimby, F. W., Barthold, S. W., Newcomer, C. E., Smith, A. L., Eds.; Elsevier: Amsterdam, 2007; Chapter 2, pp 23−XVI. DOI: 10.1016/B978-012369454-6/50056-X.

(95) Zhang, Y.; Huo, M.; Zhou, J.; Xie, S. PKSolver: An add-in program for pharmacokinetic and pharmacodynamic data analysis in Microsoft Excel. *Comput. Methods Programs Biomed.* **2010**, *99* (3), 306−314.